Turing pattern formation on the sphere for a morphochemical reaction-diffusion model for electrodeposition

Deborah Lacitignola[a,*], Benedetto Bozzini[b], Massimo Frittelli[c], Ivonne Sgura[c]

[a] *Dipartimento di Ingegneria Elettrica e dell'Informazione, Università di Cassino e del Lazio Meridionale, via Di Biasio, I-03043 Cassino, Italy*

[b] *Dipartimento di Ingegneria dell'Innovazione, Università del Salento, via per Arnesano, I-73100 Lecce, Italy*

[c] *Dipartimento di Matematica e Fisica "Ennio De Giorgi", Università del Salento, Lecce, Italy*

Abstract

The present paper deals with the pattern formation properties of a specific morpho-electrochemical reaction-diffusion model on a sphere. The physico-chemical background to this study is the morphological control of material electrodeposited onto spherical particles. The particular experimental case of interest refers to the optimisation of novel metal-air flow batteries and addresses the electrodeposition of zinc onto inert spherical supports. Morphological control in this step of the high-energy battery operation is crucial to the energetic efficiency of the recharge process and to the durability of the whole energy-storage device. To rationalise this technological challenge within a mathematical modelling perspective, we consider the reaction-diffusion system for metal electrodeposition introduced in [Bozzini et al., J. Solid State Electr.17, 467–479 (2013)] and extend its study to spherical domains. Conditions are derived for the occurrence of the Turing instability phenomenon and the steady patterns emerging at the onset of Turing instability are investigated. The reaction-diffusion system on spherical domains is solved numerically by means of the Lumped Surface Finite Element Method (LSFEM) in space combined with the IMEX Euler method in time. The effect on pattern formation of variations in the domain size is investigated both qualitatively, by means of systematic numerical simulations, and quantitatively by introducing suitable indicators that allow to assign each pattern to a given morphological class. An experimental validation of the obtained results is finally presented for the case of zinc electrodeposition from alkaline zincate solutions onto copper spheres.

Keywords: Reaction-diffusion, Turing Patterns, Surface finite elements, IMEX Euler, Electrodeposition, Battery modelling, Pattern classification

*Corresponding author

Email address: d.lacitignola@unicas.it (Deborah Lacitignola)

POST-PRINT version of the publication:
Communications in Nonlinear Science and Numerical Simulation Volume 48, July 2017, Pages 484-508,
https://doi.org/10.1016/j.cnsns.2017.01.008
https://www.sciencedirect.com/science/article/abs/pii/S1007570417300084

1. Introduction and research motivation

Safe, reliable and durable electrochemical energy storage devices, such as batteries and metal-based fuel cells, are key to the real-scale deployment of renewable energy sources. Moreover, high-energy batteries are enabling components of a multiplicity of emerging technologies such as home- and grid-storage, electric aircraft, fully electrical vehicles and telemedicine. Efficient electrochemical energy storage in batteries and regeneration of metallic fuel for fuel cells with metallic anodes critically rely on recharging capabilities. Unfortunately, such recharging and regeneration processes - that imply bulk phase formation by electrochemical reactions, or 'electrodeposition' - are currently severely limited by growth instabilities. Such instabilities lead to progressive energy losses as a function of discharge-charge cycles, device lifetime limitation as well as, in some technologies such as lithium-based ones, to severe safety hazards. More specifically, the improvement of these devices demands to face the notable challenge represented by the development of metal growth processes that prevent irregular material distribution in general and the formation of outgrowth features, such as dendrites, in particular. Over the last 40 years, this problem has been attacked with a variety of experimental and theoretical approaches but - notwithstanding the recently revived interest in metal-air technologies, that is currently producing a systematically increasing corpus of high-level literature - no definitive solution has been found.

The focus of this paper is on mathematical modelling and it is worth briefly recalling here - without any claim of completeness - some of the most representative approaches to the modelling of electrochemical dendrite formation that have been described in the literature, apart from our reaction-diffusion based that has been detailed in [9, 10, 42] and that henceforth we shall refer to as the "DIB model". Early work based on phenomenological kinetics proposed that dendrite growth was controlled by electrokinetic activation [24], but this view was later corrected by considering the interplay between activation and diffusion control [56] and references therein). This simple, but physically transparent framework allows to replace the description of mass-transport in terms of diffusion formalism with more insightful models, such as the joint density functional method, that has recently inspired physically novel approaches to the suppression of dendritic growth [44]. Moreover, instabilities related to nanocluster aggregation have been recently modelled on the basis on classical nucleation theories, combining diffusive mass transport and simple geometrical assumptions [23].

Among approaches based on a statistical description of phase formation, the diffusion-limited aggregation model was used to simulate the zinc electrodeposition process in 1D [18] and a kinetic Montecarlo approach has been proposed, assigning position-dependent van der Waals and electrochemical energies to individually depositing zinc atoms [45]. On the differential modelling side, instead electrodeposition instabilities were investigated by extending the Mullins-Sekerka instabilities theory to the electrochemical case, considering the buildup of electrochemical potential gradients [40]. This approach has been expanded to a reaction-diffusion model for two chemicals, [17]. More recently, phase-field theories, that add a variable describing the electrode-electrolyte interface as a diffuse quantity, have been proposed for the modelling of Zinc (Zn) dendrite formation [19, 71].

Finally, it is worth mentioning that Zn morphology has been correlated to, rather than modelled with, the current density distribution. This quantity has been evaluated by multi-

physics PDE modelling, incorporating ionic transport by diffusion, migration and convection, phenomenological charge-transfer kinetics and Navier-Stokes equations [72]. Electrodeposition on spherical particles in a range of spouted- and fluidised-bed configurations has been described, chiefly in the field of metal recovery from wastewater streams, e.g. [11] and references therein. Research focus in the field is generally on the precise evaluation of the current density distribution as a function of the operating conditions and, apart from special research motivations [8], electrodeposit morphology is typically neglected owing to the limited thicknesses of the coatings of practical interest in the relevant technologies. Nevertheless, very recently, the technological importance of the recovery of Zn from discharge electrolytes for off-line recharging and energy storage, e.g. [14, 60] and references therein, has attracted research attention to the option of electrodepositing Zn onto electrochemically inert metallic particles, such as e.g. Cu spheres. Since, in this specific case, high thicknesses (range of hundred micron) are of interest and one would like to minimise metal loss by the formation of loose dendrites, morphological control is of notable practical importance. This point is particularly crucial, because the relevant growth process is based on alkaline zincate solutions and it is well known that smooth zinc layers cannot be electrodeposited from these electrolytes. Possible, but practically unsatisfactory approaches to the mitigation of these instability problems are on the one hand the implementation of poorly controlled and expensive pulse plating programs or, on the other hand, the use of chemically unstable, toxic and costly additives, that impose demanding bath maintenance procedures. Moreover in Zinc-air fuel cells (ZAFC) with hopper-type anodes, the optimisation of the shape and dimensions of Zn particles is still an open question [20] and mathematical tools to rationalise this aspect are highly desirable.

Unstable growth of Zn during electrodeposition from alkaline solutions onto flat electrodes has been been the object of extensive studies and the research has been recently further fuelled by the practical importance of rechargeable Zn-based batteries. The literature features some classical references, that have systematically set the phenomenological framework - reviewed, among others, in [49, 56] - together with a steadily increasing number of recent contributions that is pointing out a range of new aspects of this widely investigated process, the details of which are beyond the scope of this paper [1, 23]. In particular, electrodeposited Zn exhibits a wide class of morphologies that depend in a poorly understood way on the growth rate. These can be broadly classified - in order of progressive degree of instability - as 'compact', layered, dendritic, spongy and mossy: only the first type is generally regarded as desirable for battery anodes, while high-surface forms such as dendrites have been recently considered of potential interest for catalytic applications [59].

The aim of this paper is thus to analyse the problem of unstable metal electrodeposition in the framework of the DIB model extending it to the case of electrodeposition on spherical cathodes. We have shown that the DIB model is able to capture many essential aspects of electrochemical pattern formation and it is thus suitable to handle the case of Zn electrodeposition from zincate solutions in energy storage applications. More in general, our work fits in the reaction-diffusion modelling framework that is particularly compelling with regard to its ability to account for pattern formation in a variety of biological, chemical and physical situations [50], many of which can be better tackled by adopting spherical domains. In fact, a close-knit group of papers has been devoted to theoretically analyse and numerically solve

reaction-diffusion models on the surface of a sphere, e.g. [16, 33, 36, 43, 46, 48, 58, 67, 69]. It is worth noting that, among these works, as we do in the present research, the following ones explicitly refer to concrete applications: [69] considered the Turing model introduced in [3] extending its study on a fixed sphere and showed that it was able to display spatial structures reminiscent of the skeletal patterns in Radiolaria [66]; [16] investigated Turing patterns on a growing sphere motivated by the formation of structures in tumor growth; [43] showed that a specific Turing model studied on a portion of a spherical surface could exhibit patterns similar to those on lady beetles' hard wings; [33] presented a phenomenological reaction-diffusion model on the surface of a sphere and showed that it could represent cerebral cortex fold formation and reproduce pathologies related to gyri formation.

In this paper: (i) we present the DIB model defined on a spherical domain (Section 2); (ii) we derive conditions for the occurrence of the Turing instability phenomenon in terms of the system parameters by using linear stability analysis (Section 3); (iii) we present and discuss numerical methods for the integration of the DIB model on spherical domains (Section 4); (iv) we investigate the steady patterns emerging at the onset of Turing instability and show that, departing from the Turing bifurcation line, the system undergoes different morphological transitions (Section 5); (v) we focus on the morphological classes of spots, labyrinth and reversed spots and investigate by systematic numerical simulations how the variation of the domain size can affect pattern formation on the sphere (Section 6); (vi) we introduce and discuss quantitative indicators that allow to assign each pattern to a given morphological class (Section 7); (vii) we present an experimental validation of the obtained results by considering the electrodeposition of Zn from alkaline zincate solution onto Copper (Cu) spheres (Section 8).

2. The DIB model

Let us consider the reaction-diffusion system (DIB model) proposed in [10],

$$\frac{\partial \eta}{\partial t} = \Delta_* \eta + \rho\, f(\eta, \theta), \qquad \frac{\partial \theta}{\partial t} = d\Delta_* \theta + \rho\, g(\eta, \theta), \tag{1}$$

which describes the spatiotemporal dynamics of the morphology $\eta(\mathbf{x}, t)$ and of the surface chemistry $\theta(\mathbf{x}, t)$ on a two-dimensional domain Ω during the electrodeposition process. $\eta(\mathbf{x}, t) \in \mathbb{R}$ is dimensionless and expresses the displacement from the instantaneous average electrodeposit plane; the dimensionless variable $\theta(\mathbf{x}, t)$, $0 \leqslant \theta(\mathbf{x}, t) \leqslant 1$, is the surface coverage with the functionally crucial adsorbate; $d = D_\theta / D_\eta$ is the ratio of the diffusion coefficients for the individual chemical and morphological processes, respectively. The strictly positive parameter ρ can have the following interpretations: (i) ρ represents the relative strength of the reaction terms with respect to the diffusion ones; (ii) increasing ρ can be thought as equivalent to decreasing the diffusion coefficient d [50]; (iii) ρ is a scale factor proportional to the area of the two-dimensional domain Ω.

The nonlinear source terms that account for generation (deposition) and loss (corrosion) of the relevant material are given by

$$\begin{aligned} f(\eta, \theta) &= A_1\,(1-\theta)\,\eta - A_2\eta^3 - B\,(\theta - \alpha)\,, \\ g(\eta, \theta) &= C\,(1 + k_2\,\eta)\,(1-\theta)\,[1 - \gamma\,(1-\theta)] - D_1\theta\,(1 + \gamma\theta)\,(1 + k_3\eta)\,, \end{aligned} \tag{2}$$

with $D_1 = \dfrac{C(1-\alpha)(1-\gamma+\gamma\alpha)}{\alpha(1+\gamma\alpha)}$.

The source term f can be thought as $f(\eta,\theta) = f_{loc}(\eta) - f_{chem}(\eta,\theta)$ namely as a balance between the localisation of the electrodeposition process and the effects of surface chemistry on the electrodeposition rate. More precisely:
$A_1(1-\theta)\eta$ accounts for the charge-transfer rate at sites free from adsorbates;
$A_2\eta^3$ describes mass-transport limitations to the electrodeposition process and
$-B(\theta-\alpha)$ quantifies the effect of adsorbates on the electrodeposition rate.
The parameter $0 < \alpha \leqslant 1$ indicates that adsorbates can have both inhibiting and enhancing effects on the growth rate. The source term g can be regarded as $g(\eta,\theta) = C\, g_{ads}(\eta,\theta) - D\, g_{des}(\eta,\theta)$ and features adsorption (parameter C) and desorption (parameter D) terms including both chemical (expanded to second order) and electrochemical (first order) contributions. Full details about the derivation and the physico-chemical meaning of the source terms can be found in [10].

In [10], we considered model (1)-(2) defined on the planar domain $\Omega = [0, L_x] \times [0, L_y]$, with L_x, L_y characteristic lengths of the electrode. We also required (1)-(2) to be supplemented by zero-flux boundary conditions and the following initial conditions:

$$\eta(x,y,0) = \eta_0(x,y), \quad \theta(x,y,0) = \theta_0(x,y), \quad (x,y) \in [0,L_x] \times [0,L_y]\,.$$

In this planar case - where $\Delta_* = \Delta = \frac{\partial^2}{\partial^2 x} + \frac{\partial^2}{\partial^2 y}$ is the classical Laplace operator- we showed that model (1)-(2) can exhibit spiral wave behaviour in a region of the parameter space where the system undergoes a Hopf bifurcation for the kinetics and that an interesting mechanism of spirals break up can also occur [41]. In addition, spatial pattern formation was also found and related to the Turing instability mechanism whereas the interplay between the Hopf and Turing instabilities was recognised as responsible for the arising of a class of spatio-temporal patterns in the neighborhood of the codimension-two Turing-Hopf bifurcation point [42]. However, factors such as changes in the domain geometry or size, that are crucial in a wide range of applications, have been not yet considered for the morphochemical model (1)-(2). A very interesting situation is when the domain Ω corresponds to a 3D surface embedded in $\mathbb{R}^3$, say $\Omega = \Gamma \subset \mathbb{R}^3$. In this case the operator $\Delta_* = \Delta_\Gamma$ is the Laplace-Beltrami operator (for more details see next Section 4) and the domain has no border, that is $\partial\Gamma = \oslash$, so that no boundary conditions have to be assigned. This case can be further enriched in realism by considering Ω as a growing domain $\Omega(t)$ so that the morphochemical model (1)-(2) becomes capable of including further information accounting for the rate of growth of the domain, that can be either pre-assigned or depending from the unknown variables η, θ (see e.g. [2, 55] for further details).
As a first step in this research direction, in the present study we consider (1)-(2) on the surface Γ of a fixed sphere of radius $R > 0$. As we will show in Section 4, the reaction-diffusion (RD) system on Γ will be solved numerically by means of the Lumped Surface Finite Element Method (LSFEM) applied to (1)-(2) with $\Delta_* = \Delta_\Gamma$, while in this section, we develop our theoretical analysis within the framework recently proposed by Plaza and coauthors [55] that describes the surface of interest by a regular parametrisation. To this aim, let us consider the fixed sphere of radius $R > 0$ defined by the parametrisation

$$X(\phi,\psi) = (x(\phi,\psi), y(\phi,\psi), z(\phi,\psi)) = (R\,\sin\psi\,\cos\phi, R\,\sin\psi\,\sin\phi, R\,\cos\psi)\,,$$

where $\phi \in [0, 2\pi]$, $\psi \in [0, \pi]$ with ϕ representing the longitudinal variable and ψ the latitude. Denoting with $h_1 = |X_\phi|$ and $h_2 = |X_\psi|$, it can be proved that for the RD system (1) in the unknowns $\eta = \eta(X(\phi, \psi), t)$, $\theta = \theta(X(\phi, \psi), t)$, the operator Δ_* is given by

$$\Delta_* u = \frac{1}{h_1 h_2} \left(\left(\frac{h_2}{h_1} u_\phi \right)_\phi + \left(\frac{h_1}{h_2} u_\psi \right)_\psi \right),$$

where $u = \eta, \theta$. Then, since $h_1^2 = R^2 \sin^2 \psi$, $h_2^2 = R^2$ and $h_1/h_2 = \sin \psi$, $h_1\, h_2 = R^2 \sin \psi$, we have

$$\Delta_* u = \frac{1}{R^2} \left(\frac{1}{\sin^2 \psi}\, u_{\phi\,\phi} + \frac{\cos \psi}{\sin \psi}\, u_\psi + u_{\psi\,\psi} \right). \tag{3}$$

It thus follows that we can study system (1)-(3) on a rectangular domain for $(\phi, \psi) \in [0, 2\pi] \times [0, \pi]$, completed with periodic boundary conditions for ϕ and a boundedness assumption at $\psi = 0$ and $\psi = \pi$ because of the singularity in the effective diffusion coefficients in (3) at the ψ boundaries.

As far as the spatially uniform equilibria are concerned, the RD system (1)-(3) admits the physically relevant spatially homogeneous equilibrium $P_e = (\eta_e, \theta_e) = (0, \alpha)$. In this regard, we recall that in the spatially uniform case P_e can loose its stability either by transcritical or by Hopf bifurcations [42]. In the former case, the attracting equilibrium P_e loses its stability because it exchanges its stability properties with another spatially uniform equilibrium. The instability threshold for the transcritical bifurcation is $B = B_{tr}$, where

$$B_{tr} = \frac{A_1\,(1-\alpha)\,F_2(\alpha, \gamma)}{(k_2 - k_3)\,F_1(\alpha, \gamma)}, \tag{4}$$

with

$$F_1(\alpha, \gamma) = (1-\alpha)(1-\gamma+\alpha\gamma), \quad F_2(\alpha, \gamma) = \frac{2\alpha\gamma(1+\alpha\gamma-\gamma)+1-\gamma}{\alpha(1+\alpha\gamma)}. \tag{5}$$

P_e is stable for $B > B_{tr}$ and unstable otherwise. In the Hopf bifurcation case, the attracting equilibrium P_e loses its stability because a couple of complex conjugate eigenvalues of the Jacobian matrix $J^e = J(P_e)$ crosses the imaginary axis. The Hopf instability threshold is $C = C_H$ where

$$C_H = \frac{A_1\,(1-\alpha)}{F_2(\alpha, \gamma)}, \quad B > B_{tr}. \tag{6}$$

P_e is stable for $C > C_H$ whereas it is unstable otherwise. Since the Hopf bifurcation at $C = C_H$ is supercritical, for $C < C_H$ homogeneous oscillations are expected due to the presence of a stable limit cycle that surrounds the unstable equilibrium P_e.

3. Turing instability and pattern formation

In order to show the occurrence of a Turing instability in system (1)-(3) leading to spatial pattern formation, we make use of linear stability analysis. We recall that a RD system exhibits diffusion-driven instability if a homogeneous steady state is *stable* to small perturbations in the absence of diffusion, but it is *unstable* to small spatial perturbations when

diffusion is present [50]. In absence of diffusion, the stability requirement for the spatially uniform equilibrium P_e is

$$J^e_{11} + J^e_{22} < 0, \qquad J^e_{11}\, J^e_{22} - J^e_{12}\, J^e_{21} > 0, \tag{7}$$

where J^e_{ij} is the ij entry of the Jacobian matrix evaluated at the steady state P_e.
Consider now $\mathbf{w} = (\eta - \eta_e,\, \theta - \theta_e)$, as a perturbation of the steady state P_e. Linearising the RD system (1)-(3) about $\mathbf{w} = 0$, we get

$$\mathbf{w}_t = D\, \tilde{\Delta}_*\, \mathbf{w} + \rho\, J^e\, \mathbf{w}, \tag{8}$$

where the diffusion matrix D is given by

$$D = \frac{1}{R^2} \begin{pmatrix} 1 & 0 \\ 0 & d \end{pmatrix}$$

and $\tilde{\Delta}_* = R^2 \Delta_*$ with Δ_* given in (3). Solutions of equation (8) are of the form

$$\mathbf{w}(\chi, t) = \sum_k c_k\, e^{\lambda\, t}\, Y_k(\chi) \tag{9}$$

where $\chi = (\phi, \psi)$ is the spatial variable. Here $\lambda = \lambda(k^2)$ is the temporal eigenvalue and the spatial solution verifies the Helmholtz equation

$$\tilde{\Delta}_* Y + k^2\, Y = 0, \tag{10}$$

where k^2 is the spatial eigenvalue. As shown in Appendix A, the eigenfunctions of the eigenvalue problem (10) are given by the spherical harmonics:

$$Y^m_l(\phi, \psi) = L^{|m|}_l(\cos\psi)\, \exp\left(i\, m\, \phi\right), \quad m = 0, \pm 1, \pm 2, \ldots \tag{11}$$

where the positive integer number l is such that $l \geqslant |m|$ and the related eigenvalues k^2 are such that $k^2 = l\,(l+1)/R^2$. Now, to explicitly derive conditions for diffusion-driven instability, one can substitute (9) into system (8) to get $(\lambda\, I - \rho\, J^e + D\, k^2)\, Y_k = 0$. To thus obtain Y_k nontrivial solutions, λ must be a solution of the characteristic polynomial

$$\lambda^2 + \lambda \left[\frac{k^2}{R^2}\,(1 + d) - \rho\,(J^e_{11} + J^e_{22}) \right] + h(k^2) = 0, \tag{12}$$

with

$$h(k^2) = d\, \frac{k^4}{R^4} - \rho\, \frac{k^2}{R^2}\, (d\, J^e_{11} + J^e_{22}) + \rho^2\, det J^e. \tag{13}$$

For diffusion driven instability to occur, a solution of (12) must be such that $Re(\lambda) > 0$. By applying the Descartes's rule of signs to (12) it follows that, in order to obtain $Re(\lambda) > 0$, the term $h(k^2)$ must be negative for some k so that we need

$$d\, J^e_{11} + J^e_{22} > 0. \tag{14}$$

Hence, the minimum h_* of $h(k^2)$ must be negative for some k. Such a minimum is achieved for $k_*^2 = \rho\dfrac{R^2}{2\,d}\,(d\,J_{11}^e + J_{22}^e)$ and is such that

$$h_* = h(k_*^2) = -\frac{\rho^2}{4\,d}\,(d\,J_{11}^e + J_{22}^e)^2 + \rho^2\,det(J^e). \tag{15}$$

Requiring that $h_* < 0$, by (15) one obtains,

$$J_{11}^e\,J_{22}^e - J_{12}^e\,J_{21}^e < \frac{1}{4\,d}\,(d\,J_{11}^e + J_{22}^e)^2\,. \tag{16}$$

In conclusion, (7), (14) and (16) are the conditions for which diffusion driven instability can induce spatial pattern formation in system (1). When the source terms are given by (2), the Jacobian matrix J^e takes the form

$$J^e = \begin{bmatrix} A_1\,(1-\alpha) & -B \\ C(k_2-k_3)\,F_1(\alpha,\gamma) & -C\,F_2(\alpha,\gamma) \end{bmatrix},$$

with $F_i(\alpha,\gamma)$ given by (5). The set of conditions (7), (14) and (16) for diffusion-driven instability can hence be specialised as:

$$C_H < C < d\,C_H, \qquad B_{tr} < B < B_T, \tag{17}$$

where $d > 1$, B_{tr} and C_H given by (4) and (6) respectively, and the Turing threshold B_T given by

$$B_T = \frac{d^2A_1^2\,(1-\alpha)^2 + C\,F_2(\alpha,\gamma)\,[2A_1d\,(1-\alpha) + C\,F_2(\alpha,\gamma)]}{4\,d\,C\,(k_2-k_3)\,F_1(\alpha,\gamma)}. \tag{18}$$

These inequalities hence determine a region in the parameter space where formation of stationary spatial patterns is expected because of the interaction between the nonlinear reaction terms and the diffusion process, see the Turing Region $\mathcal{R}$ in Fig.1. The unstable modes are the spherical harmonics (11) with $|m| \leqslant l$, for l such that $k^2 = l(l+1)/R^2$ lies in the range

$$\tilde{k}_1^2 < k^2 < \tilde{k}_2^2, \tag{19}$$

where $\tilde{k}_{1/2}^2$ are the two roots of the equation in (13) $h(k^2) = 0$, i.e.

$$\tilde{k}_{1/2}^2 = \frac{\rho\,R^2}{2\,d}\left\{\tau_e \mp \sqrt{\tau_e^2 - 4\,d\,C\,(k_2-k_3)\,F_1(\alpha,\gamma)\,[B-B_{tr}]}\right\}, \tag{20}$$

with $\tau_e = -d\,A_1(\alpha-1) - C\,F_2(\alpha,\gamma)$. Therefore if there exists at least one l satisfying conditions (19)-(20), by starting from a random perturbation of (η_e,θ_e), system dynamics can evolve into a spatially heterogeneous pattern generated by the spherical harmonics Y_l^m with $|m| \leqslant l$. We wish to stress that, when the domain is a fixed sphere, conditions (17) for the arising of diffusion driven instability are the same as the ones derived in the case of a fixed planar domain. Hence the shape of the domain seems to have no impact on the instability thresholds. Instead, the range of the allowable eigenmodes (19) depends on the radius of the sphere. Eq. (20) shows in fact that increasing the radius R of the sphere has the effect of increasing the wavenumber for which we would expect a pattern: as a result higher mode patterns - and hence more complex patterns - are expected for larger spheres.

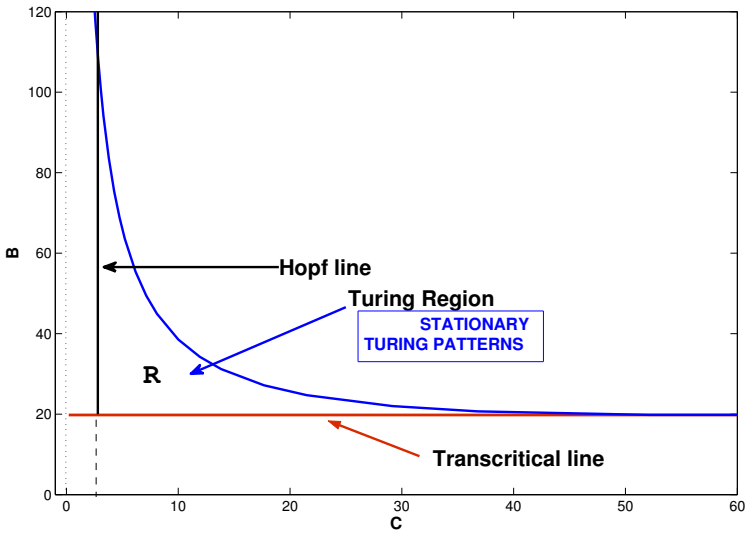

Figure 1: Turing Region in the parameter space (C, B). The values for the other parameters of the DIB model are: $\alpha = 0.5$; $\gamma = 0.2$; $k_2 = 2.5$; $k_3 = 1.5$; $A_1 = 10$; $d = 20$. The Turing region $\mathcal{R}$ is the region in the parameter space (C, B) where conditions (17) for the spatial pattern initiation are verified. Note that the Turing region does not depend on the values of A_2 and ρ.

4. Numerical Method

In Sections 5-6, we shall present several numerical simulations to describe pattern selection at the onset of instability and pattern formation depending on the size of the sphere. For this reason, in this section we briefly describe the numerical method used to solve directly on a sphere Γ of radius R the RD PDE system (1)-(2) where $\Delta_* = \Delta_\Gamma$ is the Laplace-Beltrami operator.

We perform the semi-discretisation in space by the Lumped Surface Finite Element Method (LSFEM) and the integration in time by means of IMEX Euler method that approximates implicitly the diffusion part of the PDE system and explicitly the reaction kinetics. Convergence and invariance properties of the LSFEM method, that corresponds to the version with lumping of the SFEM [26], are studied in [29]. By extending the classical FEM, Dziuk introduced the SFEM in [25] to solve the (stationary) Laplace-Beltrami equation on arbitrary surfaces in $\mathbb{R}^3$ without boundary, by providing existence/uniqueness results and error bounds. The SFEM method has then been applied to a selection of parabolic equations in [28]. The method was then extended to solve general linear elliptic equations and parabolic equations on both static and evolving domains (ESFEM) [27]. For example, the ESFEM method has been applied in [2] to solve the well-known Schnakenberg reaction-diffusion system on evolving surfaces. Other numerical approaches to solve reaction-diffusion systems on static surfaces are given, for example, in [16, 63, 68, 69].
For our purposes, here we describe the Lumped SFEM method in the case of a general $\mathcal{C}^2$ compact surface Γ in $\mathbb{R}^3$ without boundary, i.e. $\partial\Gamma = \varnothing$ for the morphochemical RD system

rewritten in matrix form as

$$\frac{\partial \mathbf{u}}{\partial t} = D\Delta_\Gamma \mathbf{u} + \mathbf{R}(\mathbf{u}), \qquad \text{for } (\mathbf{x}, t) \in \Gamma \times (0, T], \quad \mathbf{u}(0, \mathbf{x}) = \mathbf{u}_0(\mathbf{x}) \in C^2(\Gamma), \tag{21}$$

where $\mathbf{u} = \mathbf{u}(\mathbf{x}, t) = (\eta(\mathbf{x}, t), \theta(\mathbf{x}, t)) : \Gamma \times [0, T] \to \mathbb{R}^2$ is the (vector-valued) solution, D is a positive definite (diagonal) diffusion 2×2 matrix, $\mathbf{R}(\mathbf{u}) = (\rho f(\eta, \theta), \rho g(\eta, \theta))$ is the reaction term from (1) and $\Delta_\Gamma \mathbf{u} = \nabla_\Gamma \cdot \nabla_\Gamma \mathbf{u}$ is the Laplace-Beltrami operator, that is the tangential divergence of the tangential gradient $\nabla_\Gamma \mathbf{u}$ on the surface Γ (see [26]). SFEM is based on the weak formulation of (21), described by

$$\begin{aligned} &\text{find } \mathbf{u} \in (L^2([0, T]; H^1(\Gamma)))^2 \text{ with } \dot{\mathbf{u}} \in (L^2([0, T]; H^{-1}(\Gamma)))^2 \text{ such that} \\ &\int_\Gamma \frac{\partial \mathbf{u}}{\partial t} \varphi \mathrm{d}\sigma + \int_\Gamma D\nabla_\Gamma \mathbf{u} \cdot \nabla_\Gamma \varphi \mathrm{d}\sigma = \int_\Gamma \mathbf{R}(\mathbf{u}) \mathrm{d}\sigma, \\ &\forall\ t \in [0, T],\ \forall\ \varphi \in H^1(\Gamma), \forall i = 1, \dots, N \end{aligned} \tag{22}$$

where $H^1(\Gamma)$ and $H^{-1}(\Gamma)$ are Sobolev spaces on Γ and $L^2([0, T]; H^k(\Gamma))$, $k \in \{-1, 1\}$ are Bochner spaces on Γ, respectively. [2]

$\frac{\partial \mathbf{u}}{\partial t} \varphi$ is the vector-by-scalar product and $\nabla_\Gamma \mathbf{u} \cdot \nabla_\Gamma \varphi = \begin{pmatrix} \nabla_\Gamma \eta \cdot \nabla_\Gamma \varphi \\ \nabla_\Gamma \theta \cdot \nabla_\Gamma \varphi \end{pmatrix}$ is the contribution arising from the Green formula on surfaces (see [26]) applied to the Laplace-Beltrami operator.
To build the semi-discrete problem and then the approximation in space, we consider first of all a *triangulation* $\mathcal{T}_h$ of Γ given by a set of $N_T \in \mathbb{N}$ triangles $\{T_i\}_{i=1}^{N_T}$ such that:
(i) all vertices $\{\mathbf{x}_j\}_{j=1}^N$ lie on Γ and the triangulated surface is given by $\Gamma_h = \bigcup_{i=1}^{N_T} T_i$.
(ii) Γ_h is an approximation of the surface considered and it is possible to consider a one-to-one map $\mathbf{a}_{|\Gamma_h}$ between Γ and Γ_h , such that for a given function $V : \Gamma_h \to \mathbb{R}$, it is possible to define its *lift* on Γ given by $V^\ell : \Gamma \to \mathbb{R}$ such that $V^\ell(\mathbf{a}(\mathbf{x})) = V(\mathbf{x}),\ \forall \mathbf{x} \in \Gamma_h$. (For more details see [26]).
Then we consider the space of piecewise linear polynomials over Γ_h defined by:

$$S_h = \{V \in \mathcal{C}^0(\Gamma) \mid V_{|T} \in \mathbb{P}_1(T)\ \forall\ T \in \mathcal{T}_h\} \tag{23}$$

and $S_h^\ell = \{V^\ell | V \in S_h\}$ the lifted counterpart of S_h. The semidiscrete RD problem is:

$$\begin{aligned} &\text{find } \mathbf{u}_h \in (L^2([0, T]; S_h))^2 \text{ with } \dot{\mathbf{u}}_h \in (L^2([0, T]; S_h))^2 \text{ such that} \\ &\int_{\Gamma_h} \frac{\partial \mathbf{u}_h}{\partial t} \varphi_h \mathrm{d}\sigma + \int_{\Gamma_h} D\nabla_{\Gamma_h} \mathbf{u}_h \cdot \nabla_{\Gamma_h} \varphi_h \mathrm{d}\sigma = \int_{\Gamma_h} \mathbf{R}(\mathbf{u}_h) \varphi_h \mathrm{d}\sigma \\ &\forall\ t \in [0, T],\ \forall\ \varphi_h \in S_h. \end{aligned} \tag{24}$$

If $\{\mathbf{x}_j\}_{j=1}^N$ is the set of vertices in $\mathcal{T}_h$, let us choose $\{\varphi_i(\mathbf{x})\}_{i=1}^N$a basis for S_h such that, for each i, $\varphi_i(\mathbf{x}_j) = \delta_{ij}$ for all $j = 1, \dots, N$. Hence, every $\mathbf{u}_h$ in (24) may be expressed as

$$\mathbf{u}_h(\mathbf{x}, t) = \sum_{i=1}^N \boldsymbol{\xi}_i(t) \varphi_i(\mathbf{x}), \tag{25}$$

[2]The Sobolev space $H^1(\Gamma)$ is the space of functions $g : \Gamma \to \mathbb{R}$ such that, for $i = 0, 1$, the i-th order tangential derivatives, meant in a distributional sense, are $L^2(\Gamma)$. The Sobolev space $H^{-1}(\Gamma)$ is the topological dual space of $H^1(\Gamma)$. For $k \in \{-1, 1\}$, the Bochner space $L^2([0, T]; H^k(\Gamma))$ is the space of functions $u : \Gamma \times [0, T] \to \mathbb{R}$ such that $\int_0^T \|u(\cdot, t)\|^2_{H^k(\Gamma)} \mathrm{d}t < +\infty$ and $\int_0^T \|\dot{u}(\cdot, t)\|^2_{H^k(\Gamma)} \mathrm{d}t < +\infty$. (See [65].)

where for $i = 1, \ldots, N$, $\boldsymbol{\xi}_i(t) = (\xi_{\eta,i}(t), \xi_{\theta,i}(t))$ are time-dependent coefficients to be identified for the two unknown functions $\eta(\mathbf{x}, t), \theta(\mathbf{x}, t)$ of the original RD system. As usual in the finite element approach, to calculate the $\boldsymbol{\xi}_i(t)$ we consider (24) for each $\varphi_i \in S_h$ in the basis and we replace $\mathbf{u}_h$ by the expansion (25). It is worth noting that, owing to the presence of nonlinear reaction terms, the integrals $\int_{\Gamma_h} \mathbf{R}(\mathbf{u}_h)\varphi_i \mathrm{d}\sigma$ cannot be expressed in matrix form and approximation techniques must be used. In the present approach, we apply the so-called *mass lumping technique* (see for example [31, 32] for planar FEM application) and following [29] we call the resulting method as LSFEM. In analogy with [31, 32], we consider the Lagrange interpolation operator $\pi_h : \mathcal{C}^0(\Gamma_h) \to S_h$ such that for any function v on the knots $\pi_h(v(\mathbf{x}_j)) = v(\mathbf{x}_j)$ holds for all $j = 1, \ldots, N$. Then we formulate the lumped semidiscrete RD problem as:

$$\begin{aligned} &\text{find } \mathbf{u}_h \in (L^2([0,T]; S_h))^2 \text{ with } \dot{\mathbf{u}}_h \in (L^2([0,T]; S_h))^2 \text{ such that} \\ &\int_{\Gamma_h} \pi_h \left(\frac{\partial \mathbf{u}_h}{\partial t} \varphi_i \right) \mathrm{d}\sigma + \int_{\Gamma_h} D \nabla_{\Gamma_h} \mathbf{u}_h \cdot \nabla_{\Gamma_h} \varphi_i \mathrm{d}\sigma = \int_{\Gamma_h} \pi_h(\mathbf{R}(\mathbf{u}_h)\varphi_i) \mathrm{d}\sigma \\ &\forall\ t \in [0,T],\ \forall\ \varphi_i \in S_h, \forall i = 1, \ldots, N. \end{aligned} \tag{26}$$

In other words, we are approximating nonlinear integrands with their piecewise linear approximations in order to obtain an easy matrix formulation of the problem. In fact, if the semidiscrete solution $\mathbf{u}_h$ is expressed in the usual basis (25), $D = diag(d_1, d_2)$ accounts for the diffusion coefficients and f, g are the reactions components of $\mathbf{R}(\mathbf{u})$, then (26) can be written as a nonlinear ODE system of $2N$ equations as follows

$$\begin{aligned} &\widetilde{M}\dot{\boldsymbol{\xi}}_\eta + d_1 A \boldsymbol{\xi}_\eta = \widetilde{M} R_\eta(\boldsymbol{\xi}_\eta, \boldsymbol{\xi}_\theta), \\ &\widetilde{M}\dot{\boldsymbol{\xi}}_\theta + d_2 A \boldsymbol{\xi}_\theta = \widetilde{M} R_\theta(\boldsymbol{\xi}_\eta, \boldsymbol{\xi}_\theta), \\ &\text{where} \\ &R_\eta(\boldsymbol{\xi}_\eta, \boldsymbol{\xi}_\theta) = \rho \begin{pmatrix} f(\xi_{\eta,1}, \xi_{\theta,1}) \\ \vdots \\ f(\xi_{\eta,N}, \xi_{\theta,N}) \end{pmatrix}, \qquad R_\theta(\boldsymbol{\xi}_\eta, \boldsymbol{\xi}_\theta) = \rho \begin{pmatrix} g(\xi_{\eta,1}, \xi_{\theta,1}) \\ \vdots \\ g(\xi_{\eta,N}, \xi_{\theta,N}) \end{pmatrix}. \end{aligned} \tag{27}$$

The usual stiffness and lumped mass matrices are given by

$$\begin{aligned} &A_{i,l} = \int_{\Gamma_h} \nabla_{\Gamma_h} \varphi_i \cdot \nabla_{\Gamma_h} \varphi_l \mathrm{d}\sigma \qquad \forall\ i, l = 1, \ldots, N, \\ &\widetilde{M}_{i,l} = \begin{cases} \int_{\Gamma_h} \pi_h(\varphi_i, \varphi_l) \mathrm{d}\sigma & \text{if } \ i = l \\ 0 \qquad \text{if } i \neq l \end{cases} \qquad \forall\ i, l = 1, \ldots, N. \end{aligned} \tag{28}$$

The ODE system (27) is endowed with the initial condition $\boldsymbol{\xi}_\eta(0) = \boldsymbol{\xi}_\eta^0, \boldsymbol{\xi}_\theta(0) = \boldsymbol{\xi}_\theta^0$ arising from the discretisation of initial conditions $\eta(\mathbf{x}, 0), \theta(\mathbf{x}, 0)$ on the surface.
By reordering the unknowns $\boldsymbol{\xi}_\eta = (\xi_{\eta,1}, \ldots, \xi_{\eta,N})^T$, $\boldsymbol{\xi}_\theta = (\xi_{\theta,1}, \ldots, \xi_{\theta,N})^T$ in a column vector, say $\boldsymbol{\zeta} \in \mathbb{R}^{2N}$, the problem (27) may be rewritten in compact form as

$$\bar{M}\dot{\boldsymbol{\zeta}} + \bar{D}\,\bar{A}\boldsymbol{\zeta} = \bar{M} F(\boldsymbol{\zeta}), \tag{29}$$

where $F = (R_\eta^T, R_\theta^T)^T$ and $\bar{M}$, $\bar{A}$ and $\bar{D}$ are now block diagonal matrices having on the diagonals $\widetilde{M}$, A and the diffusion coefficients $d_1 I_N$, $d_2 I_N$ ($I_N \in \mathbb{R}^{N \times N}$ identity matrix),

respectively.
In our application, we will solve this ODE system by the IMEX Euler method on a uniform meshgrid of timestep $h_t > 0$, yielding the following full discrete scheme:

$$(\bar{M} + h_t \bar{D}\bar{A})\boldsymbol{\zeta_{n+1}} = \bar{M}\boldsymbol{\zeta_n} + h_t \bar{M} F(\boldsymbol{\zeta_n}), \quad n = 0, \ldots, N_t \tag{30}$$

where $\boldsymbol{\zeta_0}$ is given by the IC of the RD system. Hence in (30), two linear systems of dimension N have to be solved at each timestep $t_n = t_0 + nh_t$.

To obtain the simulations of the next sections, we implement the LSFEM/IMEX Euler method in the MATLAB environment and to solve the linear systems we apply a direct solver. The numerical solutions on the sphere for η and θ will be recovered by (25) in the polynomial basis φ_i of degree $k = 1$. In [29], it has been proved that the LSFEM/IMEX Euler method is able to preserve invariant regions of RD systems on closed compact surfaces, jointly with a counter-example showing that SFEM without lumping does not satisfy this property that is indeed important from the physical point of view. Moreover, due to the diagonal structure of mass matrix in (28), from the computational point of view the LSFEM method is less expensive than classical SFEM.

In the simulations presented in next Sections 5-6, we will show the numerical solutions obtained by the LSFEM method on the sphere for several choices of the parameters in the morphochemical model. Moreover, to appreciate the pattern distribution on the *dark side* of the sphere, we will show also the projection of each numerical solution in spherical coordinates $(\tilde{\phi}, \tilde{\psi}) \in [-\pi, \pi] \times [-\pi/2, \pi/2]$. We remark that solving the RD-PDE system directly on the sphere with our approach avoids numerical problems due to the singularity arising when the systems is instead solved on a rectangular domain in spherical coordinates, as for example in [69].

5. Pattern selection at the onset of instability

In order to gain more insight about the steady pattern that will arise at the onset of instability, the reaction-diffusion problem can be reduced to the nonlinear bifurcation equation governing the dynamics. For this purpose, general methods as the Lyapunov-Schmidt reduction [37], perturbation expansions using the Fredholm alternative [7, 21, 30, 52] or the center manifold reduction [15] can be used alternatively. In the case of a sphere, according to the center manifold approach, near a bifurcation point a physical variable of interest w is expanded in terms of spherical harmonics on a $(2l + 1)$ center manifold, such that in spherical coordinates we have $w = \sum_{m=-l}^{l} z_m(t)\, Y_l^m(\phi, \psi)$, where all the modes z_m have the same growth rate λ. In fact, differently from the case with no symmetry where only one linearly independent mode loses stability at a given set of parameter values, in the case of spherical symmetry there are $(2l + 1)$ independent modes losing stability with the same growth rate λ. The dynamics of the z_m modes are prescribed by the set of $(2l + 1)$ nonlinear ordinary differential equations that, truncated at the quadratic order, have the form:

$$\dot{z}_m = \lambda\, z_m + \beta \sum_{j,k=-l}^{l} c(j, k, m)\, z_j\, z_k, \quad m = -l, \ldots, l, \tag{31}$$

where λ is the common growth rate of the fastest growing perturbation mode obtained from the linear stability analysis of the spatially homogeneous solution; β is an arbitrary scaling parameter and the coefficients $c(j,k,m)$ are the so called Clebsch-Gordan coefficients. We refer to [47, 48, 51] for a more detailed description of the center manifold reduction procedure and for the derivation of the bifurcation equations. The equilibrium solutions of the bifurcation equations (31) correspond to steady patterns on the spherical surface for the model and the dynamics on the center manifold determines which patterns are selected - at the bifurcation - when the spatially homogeneous steady solution loses its stability. Since the bifurcation equations are $(2l+1)$, the ODE problem becomes more and more involved as l increases. However, the cases of even and odd l have been proved to be quite different [12, 13, 48]. In fact, for odd l there are no quadratic terms in the bifurcation equations whereas for even l quadratic terms are present but, because of the spherical symmetry, a unique quadratic term is allowed [48, 61]. It follows that in the case of even l, the behavior on the center manifold is uniquely determined up to the quadratic order. This is a really striking feature because - at the onset of instability - models belonging to very different contexts can generate the same type of patterns and this universality is a direct consequence of the spherical symmetry. In particular, for $l = 6, 10, 12$ it has been proved that at the onset of instability a spot pattern is selected [48].

For the case $l = 6$, analytical investigations performed in [12] have revealed that the nonlinear bifurcation equations describing the dynamics in the center manifold exhibit four solutions which have symmetry $O(2)$ (axysimmetric), I (icosahedral), O (cubic) and $D(6)$ (hexagonal). On the ground of variational principles, the icosahedral solution, i.e. with a pattern of spots, has also been indicated as the preferred one. This result has also been explained by looking at the stability properties of the different solutions in terms of the eigenvalues of the Jacobian matrix of (31). In fact, near the bifurcation, all the solutions are unstable but only the icosahedral solution has a single positive eigenvalue, while the remaining eigenvalues are negative. This solution is then preferred because it can become stable thanks to a saddle-node bifurcation if higher-order terms are considered in the bifurcation equations (31) (see [48, 61]).

The above analytical findings have been confirmed by numerical studies performed by solving different models on the surface of the sphere. For example, [69] and [16] considered two different RD systems to investigate pattern formation within the biomedical context of viruses and tumors, respectively. For the case $l = 6$, both of them found a stable spotted pattern emerging at the onset of instability for the spatially homogeneous solution. Spotted patterns were also found in [12] in a different context of convection problems. In [48], extensive investigations on the modified Swift-Hohenberg model for $l = 6$ confirmed that the spotted pattern is the one selected by the system dynamics at the onset of instability. Further numerical investigations for this model have shown that, moving away from the bifurcation boundary, a transition from an icosahedral solution with a pattern of spots to an axisymmetric striped pattern occurs and that a variety of more complicated patterns can be stable further away from the onset of the Turing instability.

For the case $l = 6$, we prove that the morphochemical model (1)-(2) shares the above *universality property* when the homogeneous steady state P_e undergoes Turing instability. Let us consider $\rho = 10$, $C = 5$ and let us fix the values of the other parameters as in Fig.1. The

eigenvalue equation (12)-(13) becomes:

$$\lambda^2 + \lambda\,(21\,b + 39.0909) - 4454.5454 + 225\,B - 910.9090\,b + 20\,b^2 = 0,$$

where $b = k^2/R^2$. The largest eigenvalue is given by

$$\lambda_+ = \lambda_+(b, B) = -10.50\,b - 19.5454 + 5\,\sqrt{h(b, B)},$$

where $h(b, B) = 3.610\,b^2 + 52.85\,b - 9\,B + 193.4$. To find specific conditions for which the largest eigenvalue λ_+ is zero, we maximize λ_+ with respect to b, by calculating $\dfrac{d\lambda_+}{db} = 0$. Then the maximum is achieved for $b_{max} = -7.3205 + 0.2908\,10^{-3}\,\sqrt{1.034 + 0.16245\,10^9\,B}$ so that $\lambda_+^{max}(B) = \lambda_+(b_{max}, B)$ can be considered as a smooth function of the parameter B. By requiring that $\lambda_+^{max}(B) = 0$, we get $B = 65.8955$ that corresponds to the Turing bifurcation threshold B_T given in (18). It follows that $b_{max} = 22.7727$ and $k^2_{max} = 22.7727\,R^2$. Hence for $B = B_T = 65.8955$, the larger eigenvalue λ_+ is zero and the other one is strictly negative and uniformly bounded away from zero, i.e. we are on the Turing curve in the bifurcation diagram. We now select the radius of the sphere so that $l = 6$ corresponds to the fastest perturbation modes growing away from the spatially homogeneous solution. Recalling that $k^2 = l(l + 1)/R^2$, we get that for $l = 6$, the value of R corresponding to the critical value of k^2 is $R_* = 1.1653$. Fig.2 shows the pattern formation process on a sphere of radius R_* for different values of the parameter B, when the other parameters are fixed as indicated before. Looking at the bifurcation diagram in Fig.1, this variation of B inside the Turing region corresponds to the decreasing of the value of B along the vertical line $C = 5$, starting from the Turing boundary ($B \approx B_T$). Fig.3 reports the corresponding solutions projected in spherical coordinates (ϕ, ψ) to emphasize the spatial structure also on the *dark side of the sphere*. Numerical results shown in Fig.2 and Fig.3 confirm the previous analytical findings. For all simulations we applied the LSFEM/IMEX Euler method with timestep $h_t = 2\ 10^{-3}$on a sphere discretization Γ_h of $N = 4098$ nodes. For $B = [65.5, 62, 57, 52, 48, 46, 44, 40, 30]$, the stationary patterns were attained at the final times $T = T(B) = [180, 90, 45, 36, 18, 18, 18, 18, 18]$. It is worth noting that in a neighborhood of the Turing bifurcation line the morphochemical model selects pattern composed of spots. Moreover, departing from the Turing bifurcation curve, the system undergoes different morphological transitions exhibiting a large variety of patterns. In fact, for B lower than B_T in turn we find: spots ($B = 65.5$, $B = 62$); stripes ($B = 57$, $B = 52$); one armed-spirals ($B = 48$, $B = 46$); again stripes ($B = 44$) and finally reversed spots ($B = 40$, $B = 30$). As insightfully discussed in [48], moving away from the bifurcation line (in our case: fixing C and decreasing the value of B within the Turing region), the transition from spotted pattern to other kinds of pattern are essentially system-dependent since, in the case of even l, the bifurcation equations that describe system dynamics on the center manifold are *universal* up to the quadratic order whereas higher order terms depend on the structure of the specific system under study. It is worth noting that, for decreasing values of B, our morphochemical model and the Swift-Hohenberg one [48, 64] exhibit some qualitative similarities in the sequence of pattern transitions. This finding would deserve further investigations, but for the moment we just point out the following facts: (i) the transition from an icosahedral solution with a pattern of spots to an axisymmetric striped pattern and (ii) the emergence

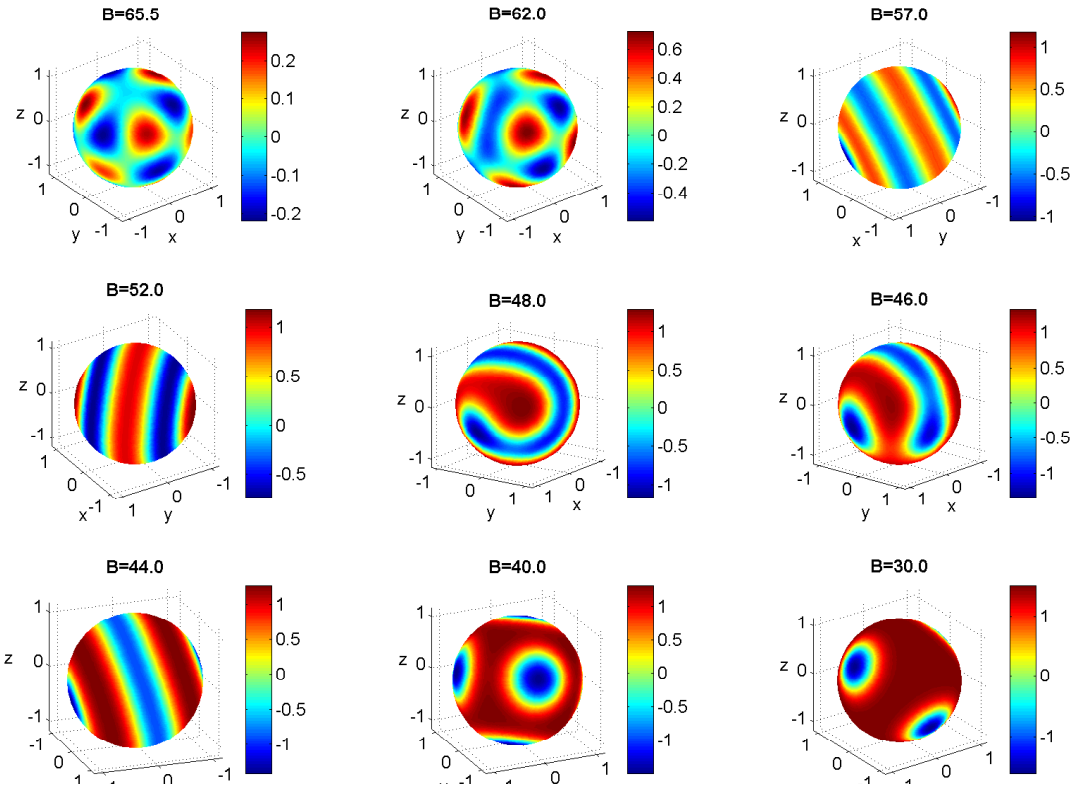

Figure 2: LSFEM numerical solutions $\eta(\mathbf{x}, T)$ of the DIB model (1)-(2) on the sphere Γ of radius $R_* = 1.1653$ with model parameters $\rho = 10$, $C = 5$ fixed and decreasing values of B starting from the Turing boundary near the threshold $B_T = 65.8955$. The other parameter values are chosen as in Fig.1. For each value of B the final time of integration T is reported in the main text. Simulations show the rich morphological transition scenarios present in the Turing region. (See also next Fig.3)

of one-armed stationary spirals after axysimmetric solutions. The latter aspect denotes an interaction between odd and even modes since these kinds of pattern only arise through a linear combinations of spherical harmonics of degrees l and $l + 1$, [64].

All the numerical results reported in this section were obtained with initial conditions $\mathbf{u}_0(\mathbf{x})$ defined in (21) prescribed as small spatially random perturbations added to the homogeneous equilibrium P_e. Keeping all the other parameters fixed, the stationary spatial patterns that emerge only depend on the initial conditions and on the value of the chosen bifurcation parameter B. In this context, it is interesting to note that, for a variety of random initial conditions and in a suitable range of the bifurcation parameter, the obtained final patterns are *qualitatively* similar from a morphological point of view so that each pattern can be considered to belong to a given *morphological* class. Hence, by using random perturbations of P_e and moving in the Turing region by only varying the bifurcation parameter B, we have found three relevant morphological classes of patterns: spots, stripes/labyrinths, reversed spots (see Fig.2 and Fig.3). These classes of patterns are worth of interest since they are ubiquitously detectable in a large variety of pattern forming systems. For example, in ecolog-

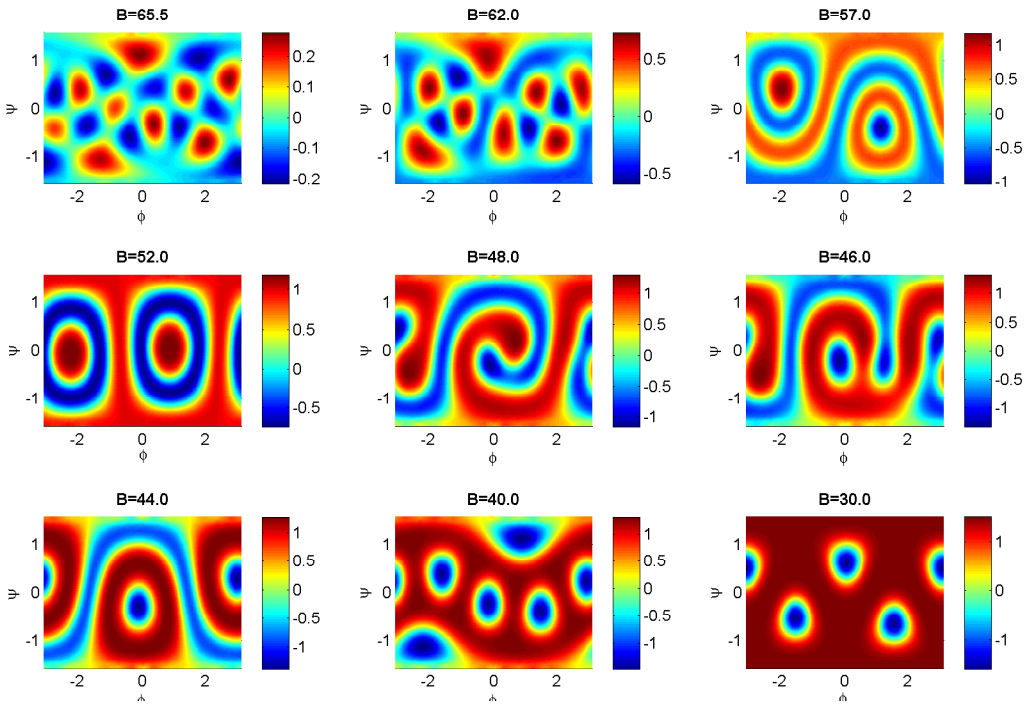

Figure 3: LSFEM numerical solutions $\eta(\mathbf{x}, T)$ of the DIB model (1)-(2): 2D view in spherical coordinates of the morphological scenarios depicted in Fig.2 for decreasing values of the parameter B in the Turing region.

ical mathematical models that describe the community scale dynamics of dryland vegetation over flat terrain [35, 57, 70], the spot, labyrinth and reversed spot (gap) patterns reflect the landscape self-organisation with respect to water resources. In particular, the transition 'gaps → labyrinths → spots' as the ecosystem aridity increases has been interpreted as an early indicator of landscape desertification [38, 39].

6. The role of the *effective* domain size on pattern formation

In Section 3, by using linear stability analysis, we found that - fixing the diffusion coefficient d and the kinetic system parameters - the range of wavenumbers yielding the arising of spatial patterns depends on the constant $\mathscr{A} = \rho R^2$ (see expressions (19) and (20)). This implies that more complex and structured patterns can be expected by increasing the value of $\mathscr{A}$. Obviously, higher values of $\mathscr{A}$ can be obtained increasing the value of ρ for a fixed value of the radius R or by increasing the sphere radius R for a fixed value of the parameter ρ. Since the surface area of the sphere Γ is $|\Gamma| = 4\pi R^2$, it is easy to see that $\mathscr{A} = \rho|\Gamma|/4\pi$ is proportional to the geometric size of the domain of integration and ρ can indeed be regarded as a scaling parameter of the surface area [50]. For our purposes, let us define $\mathscr{A} = \rho R^2$ the *effective domain size* for the PDE surface model (1).
In Section 5, the classification of patterns in terms of variation of B has been obtained for

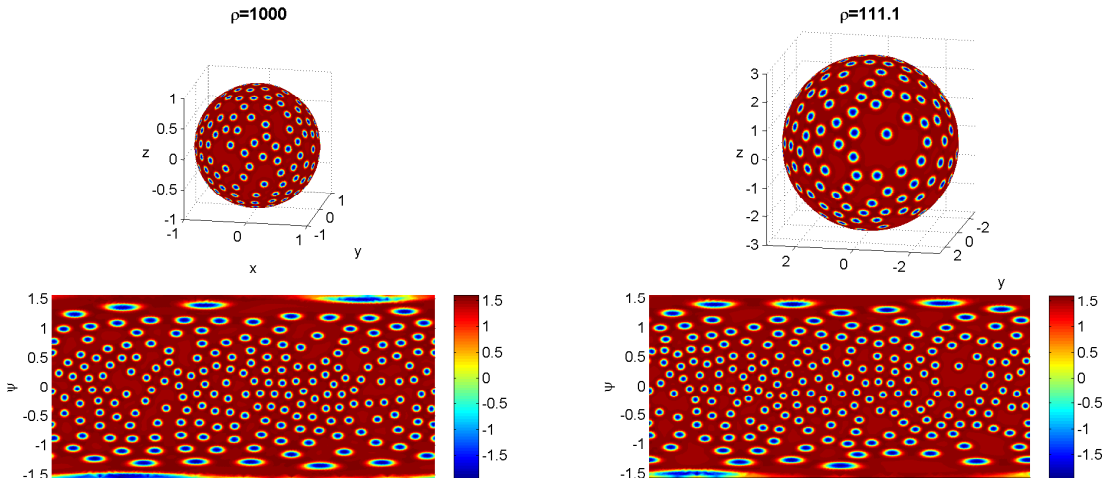

Figure 4: DIB model (1)-(2) for $(C, B) = (3, 30)$, reversed spot pattern. LSFEM numerical solutions $\eta(\mathbf{x}, T)$ for $(R_0, \rho_0) = (1, 1000)$ (left panel) and for $(R_1, \rho_1) = (3, 111.11)$ (right panel) obtained at final time $T = 1$, with timestep $h_t = 10^{-4}$ on a meshgrid of $N = 65538$ nodes. Very similar solutions are obtained on different spheres but for same effective domain size $\mathscr{A} \simeq 1000$.

$\mathscr{A} = \mathscr{A}_0 = 13.5792$. The range of unstable wavenumbers selected by (20) indicates that just few modes are present in the resulting patterns and, as confirmed in Fig.2 and Fig.3, simple structures are selected. In this section we propose a systematic numerical study of the effects of varying the effective domain size $\mathscr{A}$ on pattern formation on a sphere. To this aim, we restrict this study to three representative choices of the bifurcation parameters, prototypical of the three morphological classes identified in Section 5. In particular, we shall consider $(C, B) = (5, 62)$ for the spots, $(C, B) = (3, 66)$ for the stripes/labyrinths and $(C, B) = (3, 30)$ for the reversed spots (holes).

6.1. Fixed $\mathscr{A}$: the same morphology on spheres of different radii R

First of all we check that, keeping the value of the effective domain size $\mathscr{A}$ fixed, we can obtain the same pattern distribution on spheres exhibiting different radii R. Let us consider the parameter values $(C, B) = (3, 30)$, for which reversed spots are expected. We solve two different problems for $(R_0, \rho_0) = (1, 1000)$ and $(R_1, \rho_1) = (3, 111.11)$, such that the effective domain sizes are numerically the same $\mathscr{A}_0 = 1000 \simeq \mathscr{A}_1 = 999.99$. By the expression of $\mathscr{A}$, it is easy to see that

$$\rho_1 = \rho_0 \left(\frac{R_0}{R_1} \right)^2 \tag{32}$$

holds so that this relationship can be regarded as an effective *scaling law* among spheres of different radii R but yielding the same effective domain size $\mathscr{A}$ for the RD system.
In Fig.4 we show the numerical solutions of model (1)-(2) obtained by applying the LSFEM method (see Section 4) for the cases (R_0, ρ_0) (left panel) and (R_1, ρ_1) (right panel). The corresponding projections in spherical coordinates are also shown. The numerical results in Fig.4, obtained by the LSFEM method at final time $T = 1$ with timestep $h_t = 10^{-4}$ on a meshgrid of $N = 65538$ nodes, show that: (i) reversed spots are obtained in both cases; (ii)

even if we have two spheres Γ_0 and Γ_1 with different surface areas $|\Gamma_0| = 4\pi$ and $|\Gamma_1| = 36\pi$, the proper choice of the scaling parameters ρ_0 and ρ_1 allows to fit the *same* number of structures in these geometrically different areas. Note that, point (ii) above can be viewed as a numerical validation of the analytical results about the range of unstable modes in (20) discussed in Section 3, since in both cases the theory predicts that the *same* number of unstable modes will be present in the solution. In Section 7, we shall introduce a range of indicators capable of providing also a quantitative corroboration of this equivalence.

6.2. Effects of varying $\mathscr{A}$ by varying ρ

In the present section, we study the impact on pattern morphology of varying the *effective domain size* $\mathscr{A}$. To this aim, we have kept fixed the actual geometry - that is the radius R of the sphere - and increased the value of ρ. In the following we shall present numerical simulations obtained by: (i) fixing $R = 3$; (ii) considering the set of bifurcation parameters (C, B) representative of the three morphological classes reported in Section 5 and (iii) selecting the following ρ values, $\rho = 1, 10, 56, 100, 150, 300$. In the case of labyrinths we shall also include additional ρ values, in order to better emphasize the rich scenario of spatial structures prevailing in this case. Our choice of varying $\mathscr{A}$ by increasing ρ instead of R (i.e. instead of considering increasingly larger spheres) has a specific computational motivation. In fact, for fixed ρ, increasing the radius of the sphere Γ would imply using progressively finer space meshsizes, in order to achieve an adequate approximation $\Gamma_h \approx \Gamma$ by an appropriate triangulation. Of course, this would imply to increase the dimension $2N$ of the ODE system in (29), resulting in a notably larger computational effort to apply the full discrete IMEX method in (30), with a fixed timestep h_t. Instead, by fixing the sphere radius R a (sufficiently large) value of N can be fixed, whereby by increasing ρ only the stiffness of the corresponding ODE system (29) is increased, but not its dimension. As a result of this, the IMEX scheme in (30) must be simply applied with a (sufficiently) small timestep h_t. Small timesteps h_t, say $\leqslant 10^{-3}$, imply that a large number $N_t \simeq T/h_t$ of linear systems have to be solved in (30) until the final time of integration T. On the other hand, larger values of ρ imply faster transients in the solution, that is smaller T can be considered. Hence, in order to optimise the computational effort, for the following simulations we adopt this second strategy and we consider in the more expensive case $N = 262146$, $h_t = 10^{-5}$. Note that, for large values of ρ we consider fine meshsizes on $|Gamma_h$, that is larger N, to be able to capture the corresponding more involved pattern structures. For the LSFEM simulations for each parameter set (C, B), we will report the details of the algorithm settings as $(\rho, T(\rho), h_t, N)$, i.e. in dependence of ρ the values of the final time of integration $T = T(\rho)$, the timestep and the degrees of freedom N for the LSFEM method applied.

Fig.s 5-6-7 show the numerical simulations obtained by solving the DIB model (1)-(2) on a sphere of radius $R = 3$ for the three choices of the bifurcation parameters (C, B) reported above. In the first case, we have spot patterns, in the second one labyrithine patterns and in the third one patterns consisting of reversed spots (holes) in a flat surface. By increasing ρ, that is by increasing the effective domain size $\mathscr{A}$, the number of unstable modes (20) present in the solution increases and progressively more structured patterns develop. Fig. 5 concerns the case of spots and shows that for larger effective domain sizes, more and more spots of smaller size are present at the stationary state. It is worth noting that for this

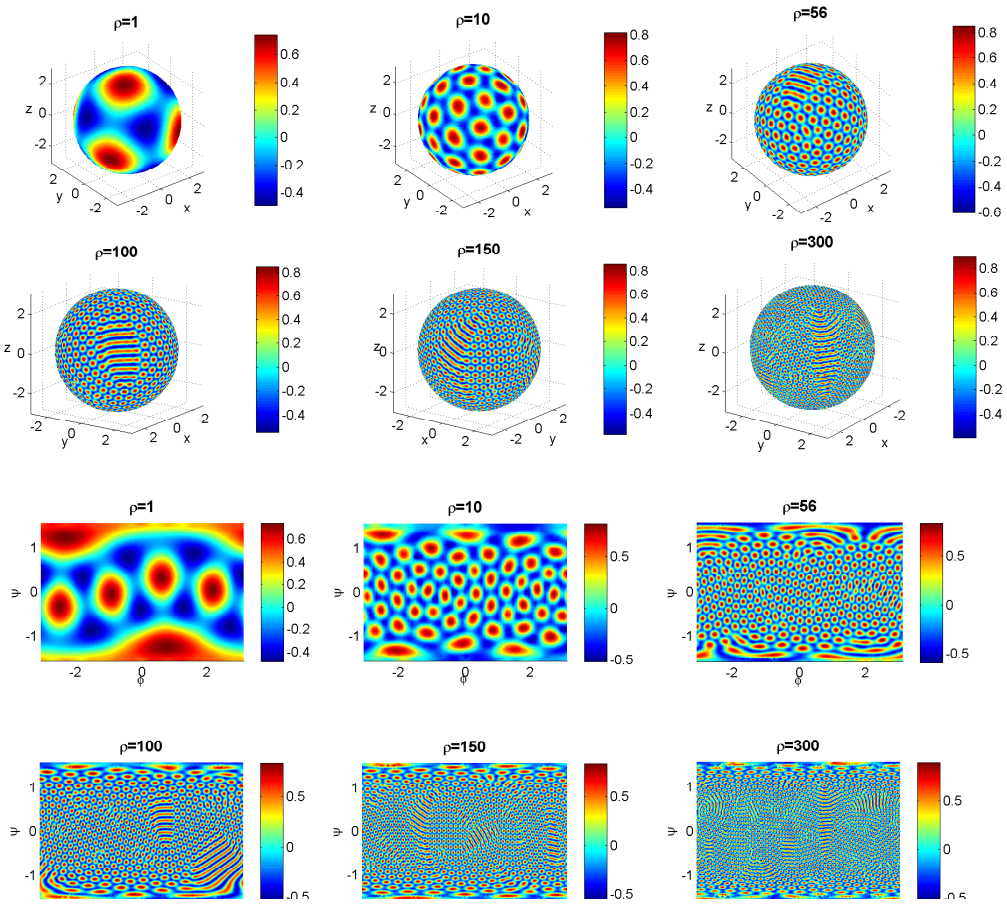

Figure 5: DIB model for $(C, B) = (5, 62)$, spot patterns on the sphere of radius $R = 3$: LSFEM numerical solutions $\eta(\mathbf{x}, T)$ for $\rho = [1, 10, 56, 100, 150, 300]$ attained at the corresponding final integration times $T = T(\rho) = [180, 90, 27, 22.5, 18, 3.6]$ (for further algorithm details see the main text). Snapshots from top left to bottom right show the morphological changes of the spot pattern on the sphere due to the variation of the effective domain size. Corresponding projections are shown in the bottom panels.

choice of parameter values, near the boundary of the Turing region, the stationary states are attained for very longtime. For this reason, we suppose that some short *stripes* present among the spots, for $\rho \geqslant 56$ are indeed *trains of spots* that have not been able to split completely at the (even long) final time of integration of our simulations. In this case, the LSFEM numerical simulations have been obtained by using the following algorithm settings $(\rho, T(\rho), h_t, N)$: $\rho = [1, 10, 56, 100, 150, 300]$, $T = [180, 90, 27, 22.5, 18, 3.6]$, $h_t = [2\ 10^{-3}, 2\ 10^{-3}, 10^{-3}, 5\ 10^{-4}, 2\ 10^{-4}, 10^{-4}]$, $N = [4098, 4098, 16386, 65538, 65538, 65538]$.

As far as the labyrinthine patterns is concerned, Fig. 6 shows that increasing ρ, the branches corresponding to the maxima (in yellow) increase in number and become thinner and more curved but they are always larger than the branches corresponding to the minima (in red). Moreover, the maximum and minimum values increase proportionally in height and depth so that uniform spatial pattern oscillations are obtained. In this case,

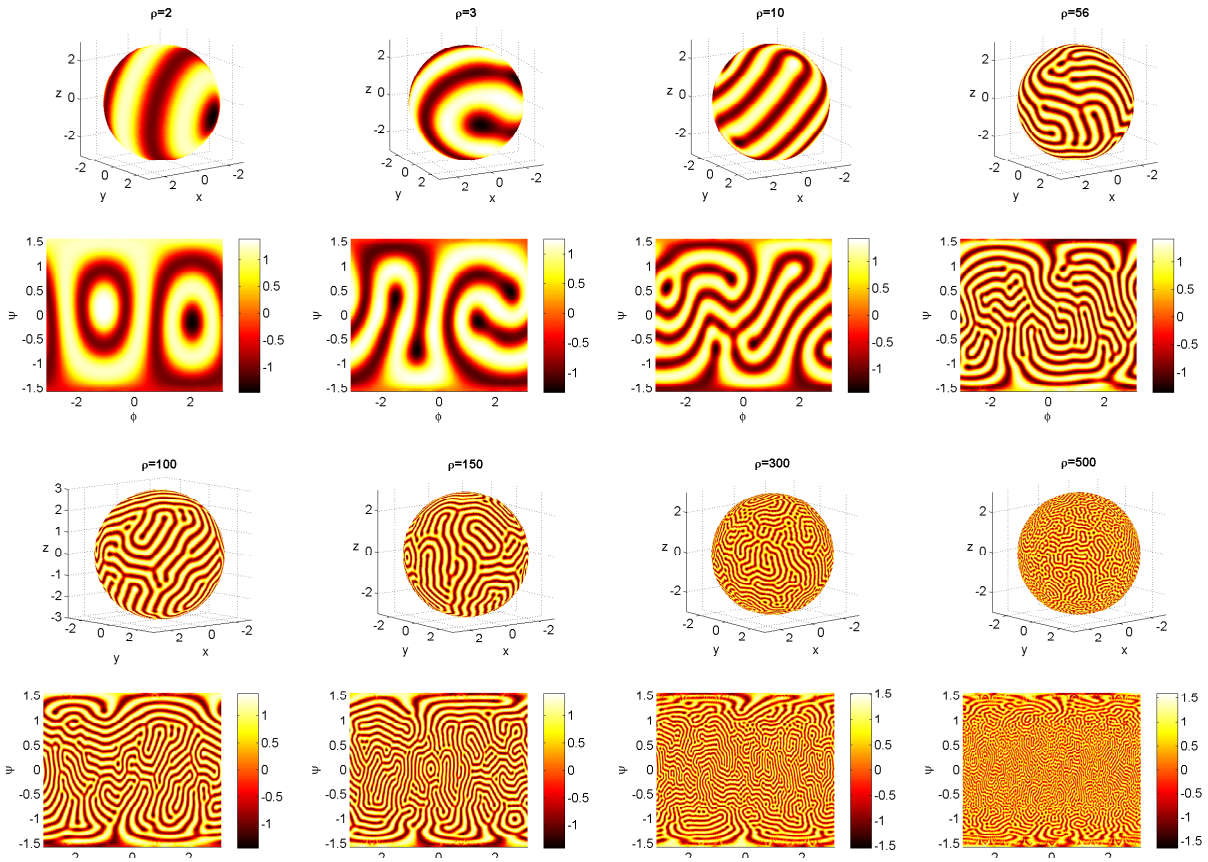

Figure 6: DIB model for $(C, B) = (3, 66)$, labyrinth patterns on the sphere of radius $R = 3$: LSFEM numerical solutions $\eta(\mathbf{x}, T)$ for $\rho = [2, 3, 10, 56, 100, 150, 300, 500]$ attained at the corresponding final integration times $T = [45, 27, 9, 4.5, 2, 2, 0.9, 0.1]$ (for further algorithm details see the main text). Snapshots from top left to bottom right show the morphological changes of the labyrinths - on the sphere and in the corresponding projection - due to the variation of the effective domain size.

the LSFEM numerical simulations have been obtained by using the following algorithm settings $(\rho, T(\rho), h_t, N)$: $\rho = [2, 3, 10, 56, 100, 150, 300, 500]$, $T = [45, 27, 9, 4.5, 2, 2, 0.9, 0.1]$, $h_t = [5\ 10^{-3}, 5\ 10^{-3}, 2\,10^{-3}, 5\ 10^{-4}, 2\ 10^{-4}, 2\ 10^{-4}, 5\ 10^{-5}, 10^{-5}]$, $N = 16386$ for $\rho = 2, 3$ otherwise $N = 65538$.

In the last case, for increasing values of ρ the reversed spots on the sphere increase in number and become progressively of smaller size and *deeper*. The maximum value corresponds to the flat surface (the red colour in Fig.7) and is essentially insensitive to changes in ρ, whereas the minima in the holes grow larger with increasing ρ. In this case, the LSFEM numerical simulations have been obtained by using the following algorithm settings $(\rho, T(\rho), h_t, N)$: $\rho = [1, 10, 56, 100, 150, 300]$, $T = [27, 9, 4.5, 1, 1, 0.9]$, $h_t = [5\ 10^{-3}, 5\ 10^{-3}, 5\ 10^{-4}, 10^{-4}, 10^{-4}, 10^{-4}]$, $N = 16386$ for $\rho = 2, 3$, $N = 262146$ for $\rho = 300$, otherwise $N = 65538$.

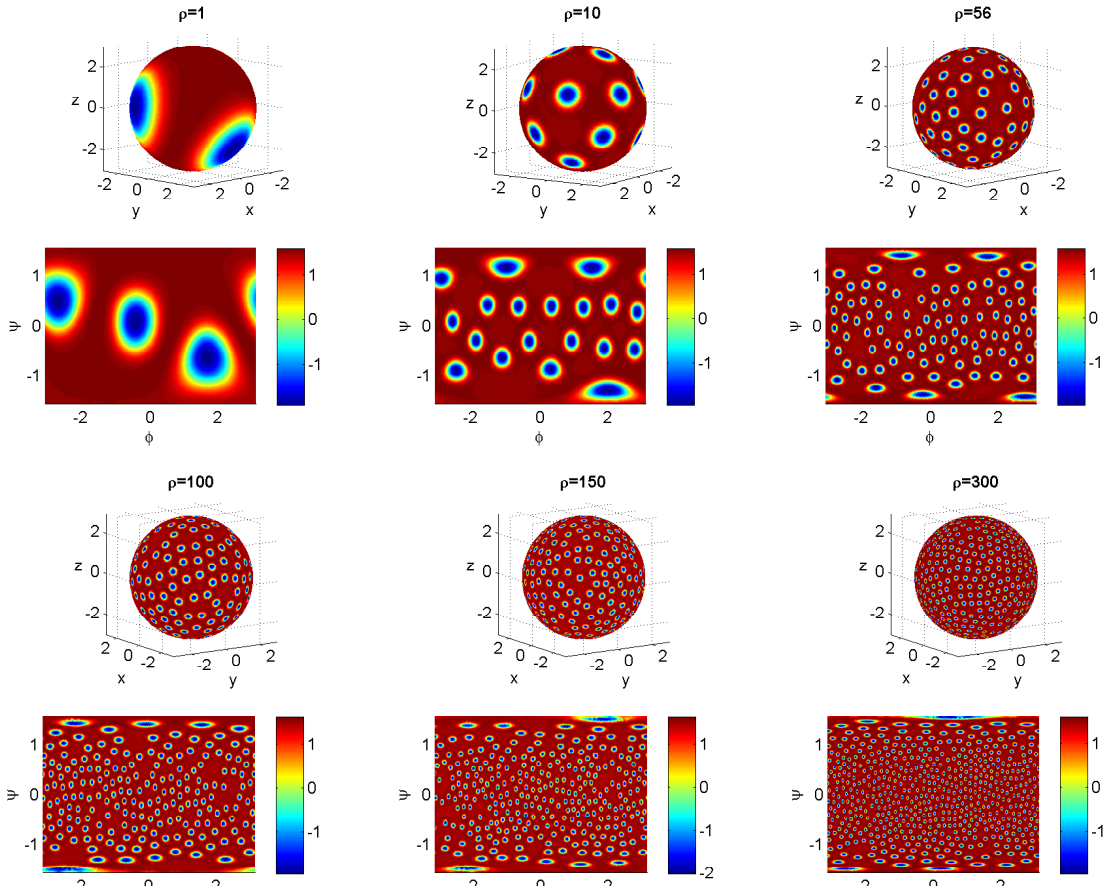

Figure 7: DIB model for $(C, B) = (3, 30)$, reversed spots (holes) on the sphere of radius $R = 3$: LSFEM numerical solutions $\eta(\mathbf{x}, T)$ for $\rho = [1, 10, 56, 100, 150, 300]$ attained at the corresponding final integration times $T = [27, 9, 4.5, 1, 1, 0.9]$ (for further algorithm details see the main text). Snapshots from top left to bottom right show the morphological changes of the patterns - on the sphere and in the corresponding projection - due to the variation of the effective domain size.

7. Pattern labelling with quantitative indicators

In this section, we introduce some quantitative indicators to classify the patterns obtained in Section 6.

7.1. Spatial mean and degree of flatness

As first indicator we consider the 'spatial mean value' of the morphology $\eta(\mathbf{x}, t)$, that is

$$\langle \eta(t) \rangle = \frac{1}{|\Gamma|} \int_{\Gamma} \eta(\mathbf{r}, t) d\mathbf{r}. \tag{33}$$

This indicator for longtime integration allows us to discriminate between stationary and oscillating patterns: if $\langle \eta(t) \rangle$ reaches an approximately constant value, a stationary pattern tends to be attained whereas an asymptotic oscillatory behaviour of $\langle \eta(t) \rangle$ indicates an

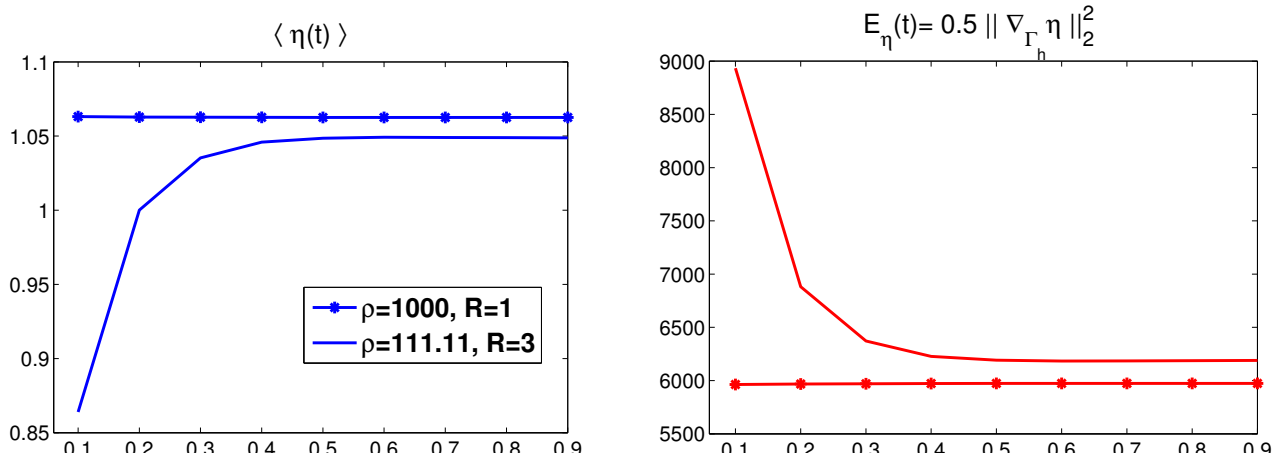

Figure 8: DIB model for $(C, B) = (3, 30)$, reversed spots. Time behaviours of the 'spatial mean' (33) and the 'degree of flatness' (34) for the solutions in Fig.4. For $(R_0, \rho_0) = (1, 1000)$ and for $(R_1, \rho_1) = (3, 111.11)$, that is same effective domain size $\mathscr{A} \simeq 1000$, the same asymptotic value is obtained: this result is a quantitative validation of the scaling law (32).

oscillating pattern.
As second indicator we consider a mean measure of the spatial gradient, that is

$$E_\eta(t) = \frac{1}{2} \|\nabla_\Gamma \eta(t)\|_2^2 = \frac{1}{2} \int_\Gamma |\nabla_\Gamma \eta(\mathbf{r}, t)|^2 d\mathbf{r} \tag{34}$$

that allows to collect information on the spatial variations of the solution. The function $E_\eta(t)$ can in fact be considered as a measure of the 'degree of flatness' of a given solution because it indicates how far the solution is from being spatially homogeneous. In fact, since for a spatially homogeneous solution $\forall \mathbf{x} \in \Gamma$, $\nabla_\Gamma \eta(\mathbf{x}) = 0$ holds, if $\lim_{t\to\infty} E_\eta(t) = \bar{E} = 0$ then no spatially inhomogeneous steady pattern exists. Whereas, if $E_\eta(t) \to \bar{E} > 0$ a spatially structured solution is attained. These indicators can be used to quantitatively confirm the results of Section 6.1 and Fig.4, that is in correspondence of different spheres but for the same effective domain size $\mathscr{A}$ the same morphochemical scenario is present. This equivalence is quantified in Fig. 8, where we show that the 'spatial mean' (33) (left panel) and the 'degree of flatness' (34) (right panel) indicators asymptotically tend to the same value for the two choices $(R_0, \rho_0) = (1, 1000)$ and $(R_1, \rho_1) = (3, 111.11)$.

7.2. Density of structures

In this section we analyse the patterns studied above in terms of the structures present in the solution for a given choice of the *effective* domain size $\mathscr{A} = R^2\rho$. We shall show that there exists a critical value of $\mathscr{A}$, say $\mathscr{A}^*$, such that for $\mathscr{A} \geqslant \mathscr{A}^*$ the emerging pattern is solely determined by the choice of the fixed bifurcation parameters (C, B) and its morphological structure is independent from the effective domain size $\mathscr{A}$. We define this particular pattern the *intrinsic pattern*. Instead, for $\mathscr{A} < \mathscr{A}^*$ there is not enough space for the pattern to completely express its *typical shape*. In contrast, we call *extrinsic patterns* those obtained

for $\mathscr{A} < \mathscr{A}^*$. Since in the cases considered in Section 6.2 we have changed the value of $\mathscr{A}$ by only changing the parameter ρ, equivalently we shall show that in our numerical simulations a critical value ρ^* exists such that the intrinsic pattern can emerge.
We first observe that, in the Turing's mechanism of pattern formation, the characteristic wavelength of the emerging pattern is solely dependent on the reaction and diffusion coefficients whereas the domain size only fixes the number of repetitions of the basic pattern that fits into the domain [53]. Hence, the total number of spots or stripes is proportional to the domain size. To express this result quantitatively, we use some tools from cluster analysis to define a density of structures for each kind of pattern identified. In the case of spots and reversed spots, it is straightforward to simply count the number of spots/holes, say $N(\rho)$ as a function of ρ. Hence, we define the *density of spots* δ_s and the *density of reversed spots/holes* δ_h by

$$\delta_s(\rho) = N_s/\mathscr{A} = N_s/(R^2\rho), \quad \delta_h(\rho) = N_h/\mathscr{A} = N_h/(R^2\rho) \tag{35}$$

Cluster analysis is applied by using some functions of the Matlab Statistics toolbox. Briefly, for each value of ρ, we define a threshold for the projected solution $\eta(\phi, \psi, T)$ to identify the locations of spots/holes as points P_k of coordinates $X_{ij} = (\phi_i, \psi_j)$ in the plane. Hence, a matrix of distances D among these points is computed, on the basis of which the same points are first pairwise grouped starting from their minimum distances and then combined into progressively larger groups in a hierarchical way. This operation is performed by using the Matlab function *Z=linkage(D)* that yields an agglomerative hierarchical cluster tree Z. The Matlab function *T=cluster(Z,'cutoff',c)* recognises the formation of a cluster when a node in the tree and all its subnodes have *inconsistency* value lower than a given threshold c. The inconsistency coefficient I characterizes each link in the tree by comparing its height with the average height of links at the same level (for leaves $I = 0$). The higher the value of I, the less similar are the objects connected by this link. Heuristically, we have chosen the cutoff c to identify the clusters as the mean value of I on our data of spots/holes. The output of the above *cluster* function is a vector T such that $n = T_k$ means that the point P_k in the data belongs to the n-th cluster identified, hence $N = max(n)$ yields the total number of clusters identified for this set of data.
We have thus used this procedure to extract the values of N_s, N_h in the above definitions of density (35) for spots and holes, respectively. In Fig.9, we report an example of cluster identification to extract the value N_h for the reversed spot solution shown in Fig.7 for $\rho = 10$ and here reported again in the upper left subplot. In Fig.9, upper right plot, we show the clusters formed by the points $P_k, k = 1, \ldots, N_P$ located in the plane by the algorithm. In Fig.9, lower left plot, we show the dendrogram of the hierarchical cluster tree Z and in Fig.9, lower right plot, the inconsistency index $I_k, k = 1, \ldots, N_P$. It is easy to see that $N_h = 20$ clusters have been identified. (Indeed 19 holes are present in the pattern solution, we found $N_h = 20$ because in the planar projection one of them is cut in two on the boundary).

For the labyrinths it is instructive to note that on the one hand very few clusters can be extracted, since the group of connected stripes generated by varying the effective domain size $\mathscr{A}$ is essentially invariant, on the other hand the width of stripes and their lengths are different. For this reason, in the case of labyrinths we define the density structure δ_l in a slightly different way, that is $\delta_l = L_m/\mathscr{A} = L_m/(R^2\rho)$, where L_m is a measure of the total length of the labyrinth. For each value of ρ, given a threshold to extract the positive values

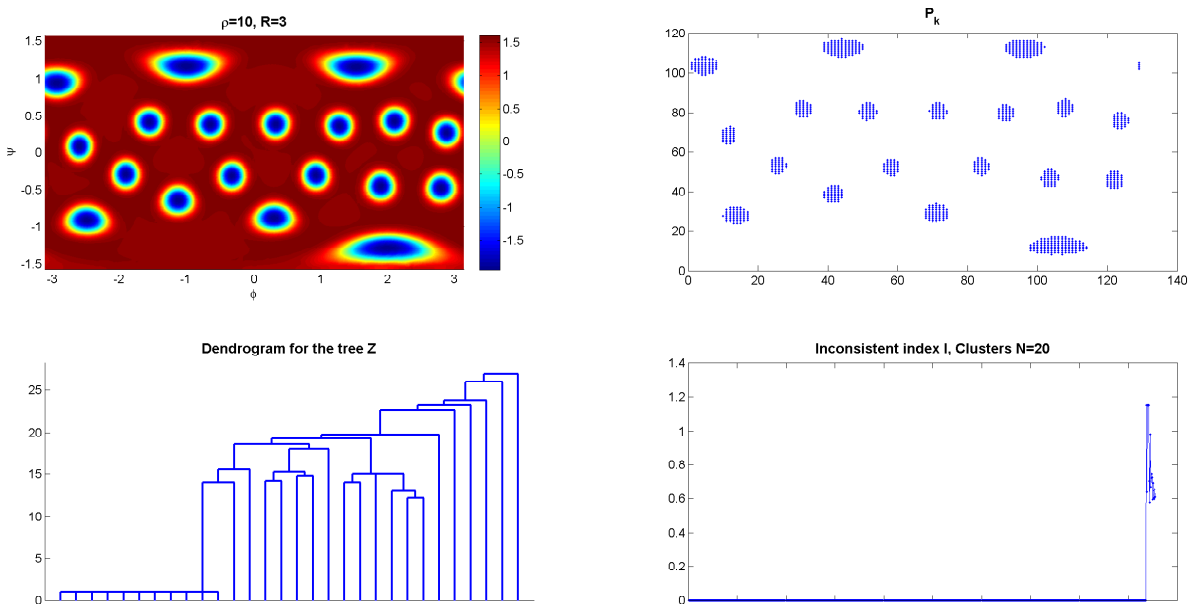

Figure 9: Cluster identification for reversed spots in the polar projection of $\eta(x, y, T)$ solution for $\rho = 10$ on the sphere $R = 3$ (see Fig.7). $N_h = 20$ clusters have been identified, indeed 19 holes are present, since in the planar projection one of them is cut in two on the boundary. See the main text for the explanation of the tree Z and of the inconsistency index I.

of the solution, we estimate L_m by calculating the area a covered by all the stripes present and their mean width w such that $L_m = a/w$.
We report the behaviour of the three structure densities $\delta_s(\rho), \delta_l(\rho), \delta_h(\rho)$ in Fig. 10. In all the cases, we found that

$$\lim_{\rho\to\infty} \delta_s(\rho) = c_s > 0, \qquad \lim_{\rho\to\infty} \delta_h(\rho) = c_h > 0, \qquad \lim_{\rho\to\infty} \delta_l(\rho) = c_l > 0,$$

that is for all kinds of patterns a constant density of structures is obtained for large values of the *effective domain size* $\mathscr{A}$. Hence, for each choice of the bifurcation parameters (C, B), we can identify the threshold value ρ^* such that we can distinguish between extrinsic and intrinsic patterns, in fact here $\rho_l^* \simeq 100, \rho_h^* \simeq 100, \rho_s^* \simeq 150$ (See Fig. 10).

7.3. Absolute and relative spatial heterogeneity

To investigate the way in which the spatial heterogeneity varies with the domain size $|\Gamma|$, we focus on the so called *heterogeneity function* that was introduced by Berding in [4] as a quantity to compare theory and experiments in parametric studies since it accounts in a simple but effective way the spatial structure of the RD patterns. In particular, Berding introduced such a *heterogeneity function* for the spatial patterns generated by RD systems with zero flux boundary conditions on a one-dimensional domain $\Omega = [0, L]$ and showed that - keeping the kinetic system parameters fixed - heterogeneity typically increases as the diffusion coefficient decreases or as the size of the diffusion domain increases.

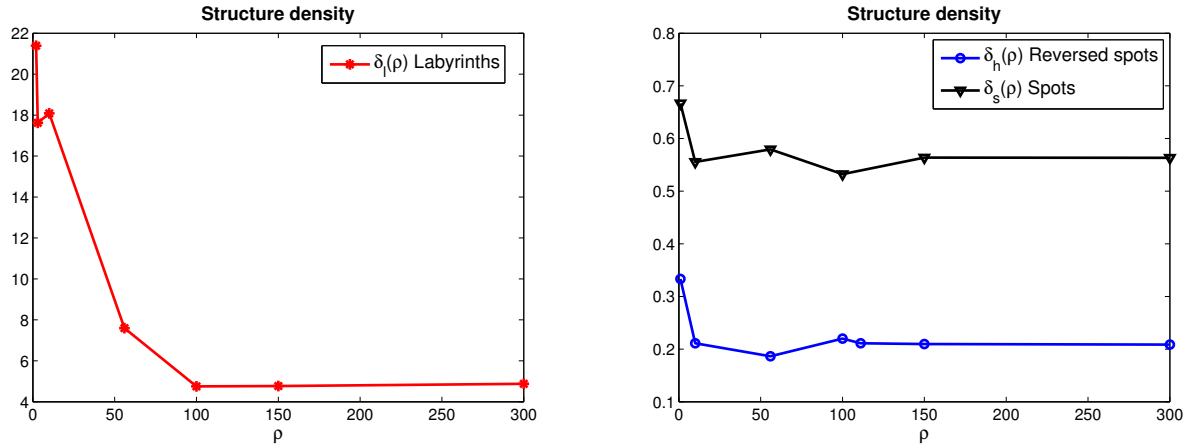

Figure 10: Structure densities $\delta_l(\rho)$ for labyrinths (left plot), $\delta_h(\rho), \delta_s(\rho)$ for reversed spots and spots (right plot). In all three morphological classes it is evident the existence of ρ^* discriminating between intrinsic ($\rho \geqslant \rho^*$) and extrinsic patterns ($\rho < \rho^*$). In fact, for $\rho \geqslant \rho^*$, that is after the critical effective domain size $\mathcal{A}^* = R^2\rho^*$, a constant density of structures is obtained.

For our specific application, after [4], the heterogeneity function can be defined as function of the scaling parameter ρ as follows

$$H(\rho) = \frac{1}{|\Gamma|}\int_{\Gamma}(|\nabla_{\Gamma}\bar{\eta}(\mathbf{x})|^2 + |\nabla_{\Gamma}\bar{\theta}(\mathbf{x})|^2)d\mathbf{x}, \tag{36}$$

where $(\bar{\eta}(\mathbf{x}), \bar{\theta}(\mathbf{x}))$ is the diffusion-driven spatially heterogeneous steady state solution of system (1)-(2) on the sphere Γ in correspondence of ρ, that is

$$\bar{\eta}(\mathbf{x}) = \lim_{t\to\infty}\eta(\mathbf{x}, t), \quad \bar{\theta}(\mathbf{x}) = \lim_{t\to\infty}\theta(\mathbf{x}, t) \quad \mathbf{x} \in \Gamma.$$

In this study we found that varying the scaling parameter ρ, $H(\rho)$ increases monotonically with ρ in a suitable parameter interval $[\rho_{min}, \rho_{max}]$. When Γ is a fixed sphere, we found that the *heterogeneity function* $H(\rho)$ displays the same theoretical trend as in the planar case. We can define the discrete version of (36) by

$$H_h^T(\rho) = \frac{1}{|\Gamma|}\int_{\Gamma_h}(|\nabla_h\bar{\eta}_h(\mathbf{x})|^2 + |\nabla_h\bar{\theta}_h(\mathbf{x})|^2)d\mathbf{x} \quad \approx H(\rho), \tag{37}$$

by using the tangential gradients on Γ_h and the numerical solutions $\bar{\eta}_h(\mathbf{x}) = \eta_h(\mathbf{x}, T), \bar{\theta}_h(\mathbf{x}) = \bar{\theta}_h(\mathbf{x}, T)$ obtained by the LSFEM method at the final time of integration T chosen such that the stationary solution is attained (see previous Section 4 for the notations). As explained in Section 4, LSFEM yields the approximation of the L_2-norm of the gradients through the stiffness matrix A in (28) such that

$$(\bar{\eta}_h^T A\bar{\eta}_h + \bar{\theta}_h^T A\bar{\theta}_h)/|\Gamma| \equiv H_h^T(\rho), \tag{38}$$

where $(\bar{\eta}_h)_j = \bar{\eta}_h(\mathbf{x}_j), (\bar{\theta}_h)_j = \bar{\theta}_h(\mathbf{x}_j)$ are the numerical solutions on the meshpoints $\mathbf{x}_j \in \Gamma_h, j = 1, \ldots, N$. It is worth noting that, by construction, (38) corresponds to the composite

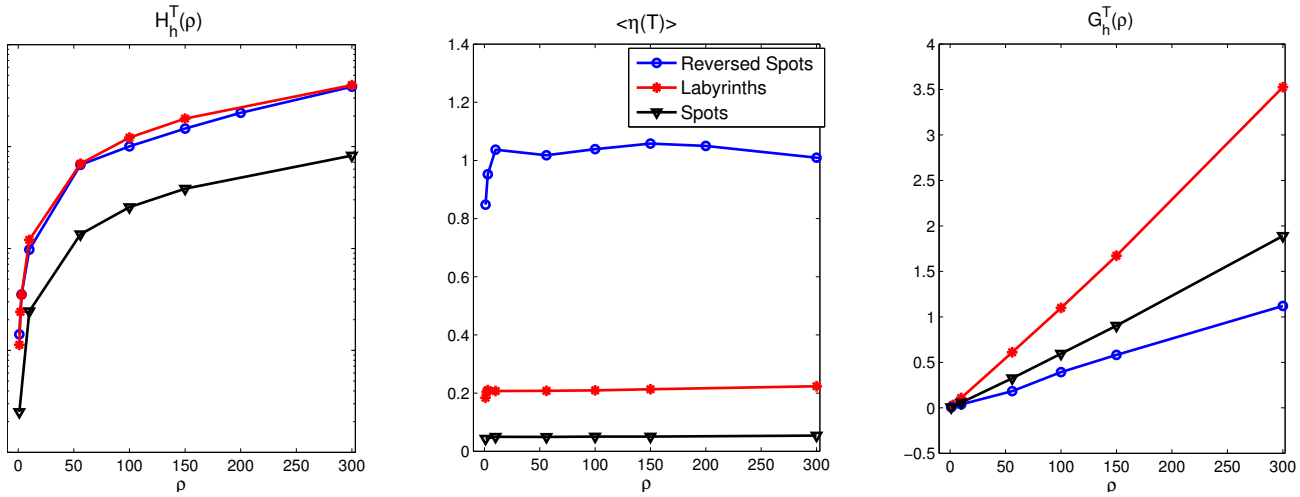

Figure 11: Morphological indicators: numerical approximations of the indicators in (36),(33),(39) evaluated for the stationary patterns reported in Fig.s 5-6-7 for increasing values of ρ obtained at the final time T. Left plot: the "heterogeneity function" $H_h^T\rho$ in (36). Middle plot: spatial mean value $\langle\eta(T)\rangle$ as function of ρ. Right plot: normalised heterogeneity $G_h^T\rho$ in (40).

midpoint quadrature rule for the integral in (37). The discretization error between $H(\rho)$ and $H_h^T(\rho)$ in (38) calculated by means of the weak formulation of the LSFEM method can be analysed as in [26] and corresponds to a second order approximation in h. Fig.11 (left) shows the discrete 'heterogeneity function' (38) $H_h^T(\rho)$ for the three pattern typologies: spots ($B = 62, C = 5$), labyrinths ($B = 66, C = 3$) and reversed spots ($B = 30, C = 3$) corresponding to the numerical solutions shown in Fig.s 5–7. In all three cases, when $\rho \in [1, 300]$, $H_h^T(\rho)$ is a monotonically increasing function of ρ meaning that higher ρ values produce spatial patterns with a higher degree of heterogeneity. In fact, numerical experiments shown in Fig.s 5-7 confirm this result, since more and more structured spatial patterns appear for larger ρ in all of the three cases considered.

In analogy with the evaluation of pattern heterogeneity, discussed above, it would be useful to be able to distinguish among the above different morphological classes on the basis of some appropriate integral indicator. To this aim, $H_h^T(\rho)$ alone is not sufficient, since it is not able to capture aspects specifically related to the pattern shape. In fact, by inspection of Fig. 11(left) one can assess that the trend of the heterogeneity function $H_h^T(\rho)$ is qualitatively the same for spots, reversed spots and labyrinthine patterns. From this point of view, the spatial mean value $\langle\eta(T)\rangle$ in (33) appears to be more effective. In fact, as shown in Fig. 11(middle), for each of the chosen patterns, $\langle\eta(T)\rangle$ (as function of ρ) is rather insensitive to changes in the parameter ρ but takes asymptotically significantly different values in correspondence of the different pattern types: ≈ 1 for the reversed spots, ≈ 0.2 in the case of labyrinths and ≈ 0.06 in the case of spots. We stress that values of $\langle\eta(T)\rangle$ approaching zero indicate a complete balance between the maximum and the minimum of the spatial oscillations of the patterns.

The above information is indeed accounted by the following function $G(\rho)$,

$$G(\rho) = \frac{H(\rho)}{\dfrac{1}{|\Gamma|}\displaystyle\int_{\Gamma} (\bar{\eta}(\mathbf{r})^2 + \bar{\theta}(\mathbf{r})^2) d\mathbf{r}}, \tag{39}$$

that was proposed in [4] to compare the ability of different models to produce spatial patterns. By following the same arguments and notations used to obtain (38) as discrete approximation of (36), we compute an approximation of (39) on the sphere as post-processing of our numerical simulations by LSFEM, then we define

$$G_h^T(\rho) = \frac{H_h^T(\rho)}{\dfrac{1}{|\Gamma|}\displaystyle\int_{\Gamma_h} (\bar{\eta_h}(\mathbf{r})^2 + \bar{\theta_h}(\mathbf{r})^2) d\mathbf{r}} \quad \approx G(\rho). \tag{40}$$

Thanks again to the weak formulation analysed in Section 4, the integral in the denominator can be calculated exactly in terms of the lumped mass matrix $\widetilde{M}$ in (28), such that we have

$$G_h^T(\rho) = \frac{\bar{\eta}_h^T A \bar{\eta}_h + \bar{\theta}_h^T A \bar{\theta}_h}{\bar{\eta}_h^T \widetilde{M} \bar{\eta}_h + \bar{\theta}_h^T \widetilde{M} \bar{\theta}_h}. \tag{41}$$

We aim to use $G_h^T(\rho)$ for classification purposes within the Turing region. From numerical investigations in the range $\rho \in [1, 300]$ we found that, for the selected patterns, $G_h^T(\rho)$ grows linearly with ρ, as shown in Fig.11 (right). As a consequence, each of the three patterns exhibits a different *heterogeneity slope*, i.e. $\dfrac{dG_h^T(\rho)}{d\rho} = constant$, that could be used as a quantitative indicator to mark out different morphological classes of patterns: the higher the slope the higher the pattern heterogeneity. In this sense, labyrinth patterns exhibit the highest degree of spatial heterogeneity and reversed spots the lowest one. This appears fully consistent with numerical simulations depicted in Fig.7 which show that reversed spots are *holes* in an essentially flat substrate.
The fact that the heterogeneity indicator G defined in (39) depends linearly on ρ, when keeping the radius of the sphere R fixed, has the same geometrical meaning as the constancy of the intrinsic pattern density keeping the effective domain area $\mathscr{A} = \rho R^2$ constant, as expounded in Section 6. In fact, if G be evaluated keeping the effective area constant, it would be independent on ρ. This can be straightforwardly shown in the case of a square domain of side L onto which square-based pyramids all of the same height h are formed. In this simple scheme, keeping L constant, ρ corresponds to the number of squares into which the domain is subdivided, that form the basis of pyramids of height h. Assuming, for simplicity that $\bar{\eta} = \bar{\theta}$, one obtains: $G(\rho) = 4\,\rho\,(h/L)^2$. Since L is constant, from the last equation one immediately finds that $\frac{dG(\rho)}{d\rho} = 4\,(h/L)^2$, while at constant effective domain area, i.e. $\mathscr{A} = \rho L^2 = k$ one gets: $G_\rho = 4\,k\,h^2/L^4$ which is independent on ρ so that $dG(\rho)/d\rho = 0$. The last equation expresses formally the constancy of intrinsic pattern density in terms of $G(\rho)$.

To sum up this section, the density structure indicator δ and the heterogeneity function $G(\rho)$ - discussed in Sections 7.2 and 7.3 respectively - have allowed to assign a given pattern to

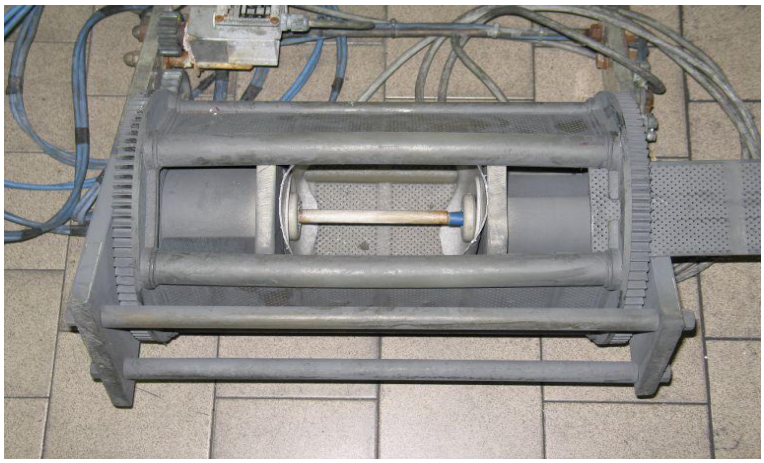

Figure 12: The laboratory rotary-barrel reactor used for Zn plating onto Cu spheres

one of three different morphological classes.
Moreover, an effective scaling law among spheres of different radii - within a given pattern class - has been validated by spatial mean and degree of flatness indicators (Section 7.1).

8. Comparison with experiments

Experimental validation of the DIB model (1)-(2) integrated on a sphere has been performed with reference to the scientific case of electrodeposition of Zn from alkaline zincate solution onto Cu spheres 2.5 mm in diameter in a laboratory rotary-barrel reactor equipped with a central Cu-bar counter-electrode (see Fig. 12). This specific example refers to an electrometallurgical process, that is key to the performance of zinc-air batteries. It is worth noting that the reactions addressed in this work are fully inorganic ones and, at variance with many studies in pattern formation, they do not refer to a biological system. Basic information on electrometallurgy and the relevant notation can be found in [56] while a description of zinc-air batteries and their chemistries, including details on the specific operation considered in the present paper, is available in [14]. Moreover, the Zn electrodeposition process implies the growth of a metal film on top of a spherical metallic support. Therefore, the problem is an intrinsically moving-domain one and a formally complete solution would require to follow the shape change of the cathode from the initially spherical one to that resulting from the patterns developing in the added metal film. Nevertheless, quantitatively, typical film thicknesses lie in the range of a few tens of microns, while support diameters are generally larger than 1 mm: the domain shape change can thus be neglected, at least for the scope of the present investigation. Of course, it would be highly interesting to generalize our metal deposition problem to the moving-domain case and we are planning to attack this problem in the near future, based on high-standard seminal work available in the literature, such as that described in [2, 55] and references therein. The electrolyte was a real spent ZAFC electrolyte containing 6 M KOH and saturated with zincates (extracted from the waste tank of a laboratory single-cell present in our laboratory). Electrodeposition was carried out potentiostatically, applying a series of cathodic overvoltages (see Fig. 13), measured against

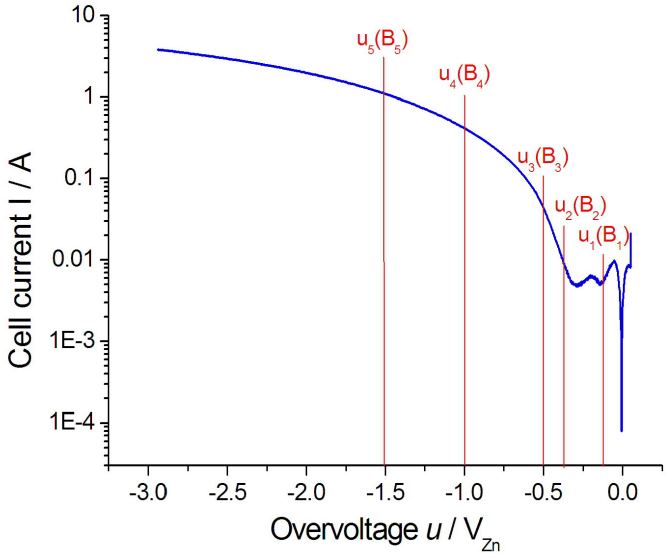

Figure 13: Linear-sweep voltammogram measured in the laboratory rotary-barrel reactor loaded with Cu spheres and operating potentiostatically (Zn reference electrode) in a saturated alkaline zincate solution. We indicated in red the overvoltages at which we carried out the electrodeposition experiments.

a Zn rod immersed in the zincate bath just outside the rotary barrel: accurate calibration of the ohmic drop was beyond the scope of the present investigation. The classical reaction system for Zn electrodeposition from zincate solution is [5, 23]:

$$\mathrm{Zn(OH)}_{4,aq}^{2-} \quad \rightleftarrows \quad \mathrm{Zn(OH)}_{2,surf} + 2\,\mathrm{OH}^- \tag{42a}$$

$$\mathrm{Zn(OH)}_{2,surf} + \mathrm{e}^- \quad \rightleftarrows \quad \mathrm{Zn\,OH}_{surf} + \mathrm{OH}^- \tag{42b}$$

$$\mathrm{Zn\,OH}_{surf} + \mathrm{e}^- \quad \rightleftarrows \quad \mathrm{Zn} + \mathrm{OH}^- \tag{42c}$$

where Eq.(42.b) is the rate determining step. The overall equation describes the reduction of oxidized Zn in the form of zincate ($\mathrm{Zn(OH)}_{4,aq}^{2-}$), stable in the typical alkaline electrolyte of a zinc-air battery to metallic Zn: this reaction represents the charging step in a zinc-air battery and in the flow-cell concept we are developing (see [6, 14] for details) is carried out in a dedicated reactor (see Fig. 12). The overall reaction goes on through three steps: (42.a) the adsorption of zincate to zinc oxide; (42.b) the one-electron reduction of adsorbed Zn(II) hydroxide to intermediate adsorbed Zn(I) hydroxide and (42.c) the one-electron reduction of surface Zn(I) metallic Zn.
From Eq.s (42) one can straightforwardly derive the set of phenomenological kinetic equations (for details on the derivation, see Appendix B):

$$\begin{cases} f_1(\theta_1,\theta_2) = \vec{k}_1\, Z(1-\theta_1-\theta_2) - \overleftarrow{k}_1\,\theta_1 - \vec{k}_2\,\theta_1 + \overleftarrow{k}_2\,\theta_2, \\ \\ f_2(\theta_1,\theta_2) = \vec{k}_2\,\theta_1 - \overleftarrow{k}_2\,\theta_2 - \vec{k}_3\,\theta_2 + \overleftarrow{k}_3, \end{cases} \tag{43}$$

where f_1 and f_2 are the reaction rates and Z, θ_1 and θ_2 - which are functions of space and time - are defined as $Z = \left[\mathrm{Zn(OH)}^{2-}_{4,aq}\right]$, $\theta_1 = \left[\mathrm{Zn(OH)}_{2,surf}\right]$, $\theta_2 = [\mathrm{Zn\,OH}_{surf}]$. The constants $\vec{k}_i, \overleftarrow{k}_i$, $i = 1, 2, 3$, are the kinetics constants in equations (42): the right arrow denotes the forward reaction, the left arrow the backward one. We have described the surface concentrations with surface fractions θ_1, θ_2 and we have formally incorporated the Zn activity in the kinetic constant $\overleftarrow{k}_3$.

The dimensional source terms exhibit the following units: $[f_1,\ f_2]$ m^{-2} s^{-1}; $[\vec{k}_1]$ mol^{-1} s^{-1}; $[Z]$ mol m^{-2}; $[\theta_1,\ \theta_2]$ 1; $[\overleftarrow{k}_1,\ \vec{k}_2,\ \overleftarrow{k}_2,\ \vec{k}_3,\ \overleftarrow{k}_3]$ m^{-2} s^{-1}. The dimensionless form of Eq. (43) can be straightforwardly obtained by using the normalization constants for space and time used for Eq. (1) and choosing a reference value of 1 mol m^{-2} for Z, as customary in metallurgical thermodynamics (e.g. [22]).

Since the corrosion rate in the relevant conditions (i.e. during electrodeposition) is negligible, one can set $\overleftarrow{k}_3 \cong 0$, hence Eq. (43) rewrites to:

$$\begin{cases} f_1(\theta_1, \theta_2) = \vec{k}_1\, Z(1-\theta_1-\theta_2) - \overleftarrow{k}_1\, \theta_1 - \vec{k}_2\, \theta_1 + \overleftarrow{k}_2\, \theta_2, \\ \\ f_2(\theta_1, \theta_2) \cong \vec{k}_2\, \theta_1 - \overleftarrow{k}_2\, \theta_2 - \vec{k}_3\, \theta_2. \end{cases} \tag{44}$$

From the experimental fact that Eq. (42.b) is the rate determining step, we can make the approximation: $\theta_2 << \theta_1$. The first equation of Eq. (44) thus rewrites to:

$$f_1(\theta_1, \theta_2) \cong \vec{k}_1\, Z(1-\theta_1) - \overleftarrow{k}_1\, \theta_1 - \vec{k}_2\, \theta_1 + \overleftarrow{k}_2\, \theta_2,$$

and from the high surface coverage with hydroxides resulting from the fact that high zincate concentrations are typical of the Zn recovery process from spent ZAFC electrolytes, one can approximate $\theta_2 \cong 1 - \theta_1$, allowing to restate the kinetic system in the form

$$\begin{cases} f_1(\theta_1) \cong \vec{k}_1\, Z(1-\theta_1) - \overleftarrow{k}_1\, \theta_1 - \vec{k}_2\, \theta_1 + \overleftarrow{k}_2\, (1-\theta_1), \\ \\ f_2(\theta_1) \cong \vec{k}_2\, \theta_1 - (\overleftarrow{k}_2 + \vec{k}_3)(1-\theta_1). \end{cases}$$

Since the rest of our deduction will be made under the steady state assumption, from now on we shall drop the $\cong$ symbols. We observe that the growth rate r of electrodeposited Zn is the opposite of that of $\mathrm{Zn\,OH}_{surf}$ consumption, f_2, so that we can write

$$r = -f_2, \tag{45}$$

hence, applying Eq. (45) and rearranging terms in view of the discussion of the physical meaning:

$$\begin{cases} f_1(\theta_1) = (\overleftarrow{k}_2 + \vec{k}_1\, Z)(1-\theta_1) - (\overleftarrow{k}_1 + \vec{k}_2)\theta_1, \\ \\ r(\theta_1) = \overleftarrow{k}_2\, (1-\theta_1) - (\vec{k}_2 + \vec{k}_3)\theta_1 + \vec{k}_3, \end{cases} \tag{46}$$

The fact that Eq. (42.b) is the rate determining step, implies the following relationships of the kinetic constants:

$$\overleftarrow{k}_1 \gg \vec{k}_2; \qquad \vec{k}_1\, Z \gg \overleftarrow{k}_2,$$

hence we can rewrite (46) in a simplified form, without loss of generality:

$$\begin{cases} r(\theta_1) = \overleftarrow{k}_2\,(1-\theta_1) - (\overrightarrow{k}_2 + \overrightarrow{k}_3)\theta_1 + \overrightarrow{k}_3, \\ \\ f_1(\theta_1) = \overrightarrow{k}_1\,Z(1-\theta_1) - \overleftarrow{k}_1\,\theta_1. \end{cases} \tag{47}$$

System (47) can be straightforwardly interpreted as a special case of the source terms of the DIB model in Eq. (2), as detailed below:

$$\begin{aligned} &\overleftarrow{k}_2 = A_1\,\eta, \quad \overrightarrow{k}_2 + \overrightarrow{k}_3 = B, \quad \overrightarrow{k}_3 = B\alpha, \\ &\overrightarrow{k}_1\,Z = C(1+k_2\eta)\left[1-\gamma(1-\theta_1)\right], \quad \overleftarrow{k}_1 = D(1+\lambda\theta_1)(1+k_3\eta\theta_1). \end{aligned} \tag{48}$$

The terms of Eq.s (42.b) and (42.c) refer to electrochemical reactions, they can be expressed in an Arrhenius form, containing an electrical activation term, that is a function of the applied overvoltage u.

$$k_i = A_i \exp\left(\frac{E_{act,i}^{electrochem}}{RT}\right) = A_i \exp\left(\frac{E_{act,i}^{chem} + E_{act,i}^{electr}(u)}{RT}\right) \tag{49}$$

hence

$$\overleftarrow{k}_2 = \overleftarrow{A}_2 \exp\left(\frac{\overleftarrow{E}_{act,2}^{chem} + \overleftarrow{E}_{act,2}^{electr}\ (u)}{RT}\right) \cong \overleftarrow{A}_2 \exp\left(\frac{\overleftarrow{E}_{act,2}^{chem}}{RT}\right) \quad \Rightarrow \ \frac{\partial\ \overleftarrow{k}_2}{\partial u} \cong 0,$$

$$\overrightarrow{k}_2 = \overrightarrow{A}_2 \exp\left(\frac{\overrightarrow{E}_{act,2}^{chem} + \overrightarrow{E}_{act,2}^{electr}\ (u)}{RT}\right) \cong \overrightarrow{A}_2 \exp\left(\frac{\overrightarrow{E}_{act,2}^{chem} - 2F\,\overrightarrow{\alpha}_2\,u}{RT}\right) := \overrightarrow{i}_{o,2} \exp\left(-\frac{u}{\overrightarrow{B}_{T,2}}\right)$$

$$\overrightarrow{k}_3 = \overrightarrow{A}_3 \exp\left(\frac{\overrightarrow{E}_{act,3}^{chem} + \overrightarrow{E}_{act,3}^{electr}\ (u)}{RT}\right) \cong \overrightarrow{A}_3 \exp\left(\frac{\overrightarrow{E}_{act,3}^{chem} - 2F\,\overrightarrow{\alpha}_3\,u}{RT}\right) := \overrightarrow{i}_{o,3} \exp\left(-\frac{u}{\overrightarrow{B}_{T,3}}\right).$$

We observe that $\overleftarrow{k}_2$ refers to an anodic process and since in our electrodeposition process we are applying cathodic conditions, it can be regarded as independent on u. Moreover, $\overrightarrow{k}_2$ and $\overrightarrow{k}_3$ can eventually be expressed in the classical Tafel form. It is worth noting that - owing to the assumptions adopted for the kinetic discussion of the electrodeposition process from a zincate bath - the formal interpretation of the DIB parameter A_1 in this context is slightly different from - though of course theoretically coherent with - the general one expounded in Section 2, where the role of u and η is in fact identified on the basis of electric field localisation effects, according to [10, 34]. Finally, by plugging (49) into the terms of (48) containing B, and assuming - without loss of generality - that $\overrightarrow{B}_{T,2} = \overrightarrow{B}_{T,3} := \overrightarrow{B}_T$, one obtains

$$B = \left(\overrightarrow{i}_{o,2} + \overrightarrow{i}_{o,3}\right) \exp\left(-\frac{u}{\overrightarrow{B}_T}\right); \qquad \alpha = \frac{\overrightarrow{i}_{o,3}}{\overrightarrow{i}_{o,2} + \overrightarrow{i}_{o,3}} \tag{50}$$

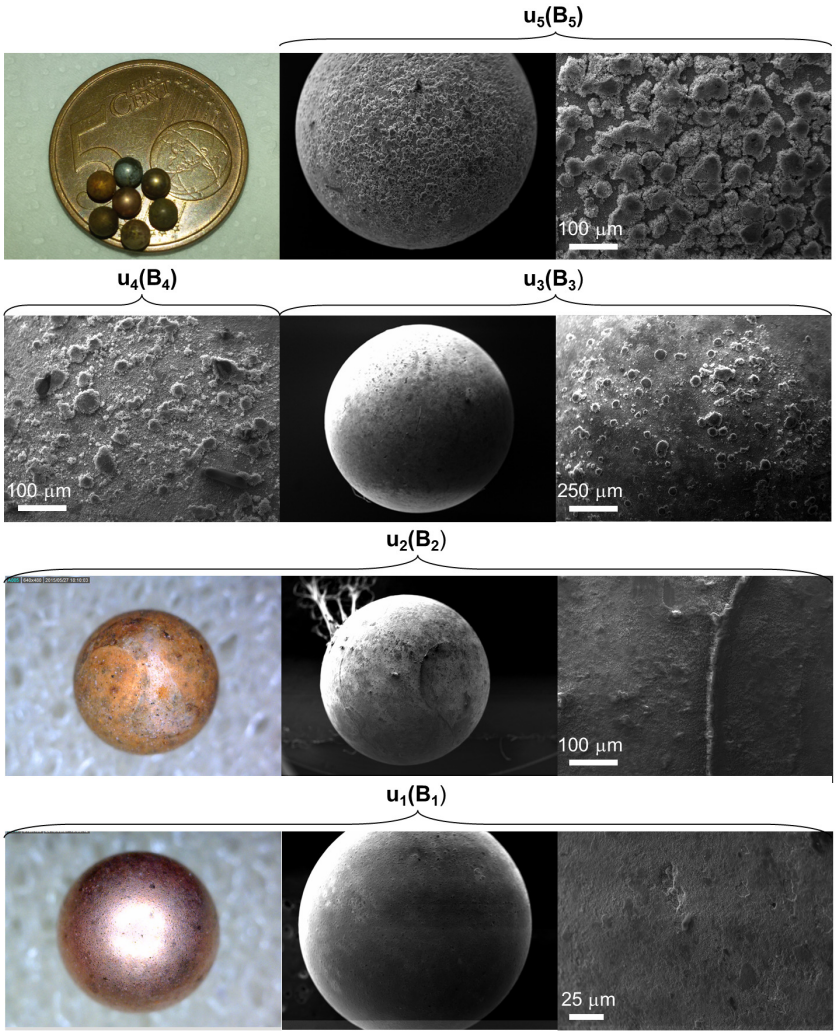

Figure 14: Optical and scanning electron micrographs of Cu spheres with Zn electrodeposits obtained potentiostatically at the overvoltages reported in Fig. 13

Therefore, the only parameter of the DIB model that is a function of u is B. In order to compare solutions of η obtained from the DIB model by varying B over a range contained in the Turing region, we have carried out a series of experiments by varying u over a range of negative values, corresponding to different applied cathodic overvoltages. Potentiostatic electrodeposition experiments were carried out at five representative overvoltages ($u = -0.125, -0.375, -0.5, -1.0, -1.5$ V) for 2 hours (see Fig. 13). Typical Zn morphologies were documented by optical and scanning electron microscopies and are reported in Fig. 14. Recalling that decreasing values of u correspond to increasing values of B, from the reported micrographs one can notice that the film grown at u_1 is relatively flat and exhibits some metal recesses (holes) on an overall flat surface; the sphere coated at u_2 exhibits bands with higher Zn content; the electrodeposits obtained at u_3, u_4 and u_5 show a nodular structure with a progressively higher density of globular grains the dimensions of which decrease with

increasing overvoltage.

In this paper we have restricted our validation to a semiquantitative, but, in our opinion, highly diagnostic level: focussing on the one hand on the interpretation of our general electrodeposition model in terms of a specific chemistry (Eq.s (42)-(48)) and on the other hand on the experimental proof of the impact of the systematic variation of a real electrochemical parameter on pattern formation. In a subsequent paper [62] we have addressed the problem of comparing quantitatively experimental patterns and model predictions with a parameter identification approach.

9. Conclusions

In this paper we have investigated the emergence of spatial organization phenomena for the morphochemical electrodeposition model introduced and experimentally validated in [10], extending its study to spherical surfaces. We have used linear stability analysis to derive conditions for Turing pattern formation. We found that, by fixing the diffusion coefficient d and the kinetic system parameters, the range of wavenumbers yielding the arising of spatial patterns depends on the constant $\mathscr{A} = \rho R^2$ that we have interpreted as *effective domain size*. By fixing the value of $\mathscr{A}$ so that the spherical harmonics of degree $l = 6$ correspond to the fastest perturbation modes growing away from the spatially homogeneous equilibrium P_e, we have shown that the morphochemical RD model (1)-(2) exhibits a stable spotted pattern emerging when the spatially homogeneous steady state P_e undergoes Turing instability. This phenomenology turns out to be perfectly in line with the general theoretical results concerning pattern formation on the surface of the sphere. We also numerically found that, decreasing the bifurcation parameter B from the Turing bifurcation curve, the system undergoes different morphological transitions exhibiting a large variety of modifications of three basic pattern classes: spots, labyrinths and reversed spots. The structures obtained by numerical integration match precisely those obtained experimentally by electrodepositing zinc onto copper spheres.
Furthermore, within each class of patterns, we have found that a critical value of $\mathscr{A} = \mathscr{A}^*$ exists, such that for $\mathscr{A} \geqslant \mathscr{A}^*$ *intrinsic* patterns emerge, namely patterns that are solely determined by the choice of the fixed bifurcation parameters and with a morphological structure independent from the value of $\mathscr{A}$. On the contrary, for $\mathscr{A} < \mathscr{A}^*$, *extrinsic patterns* arise, namely patterns that are unable to completely express their *typical shape* because they have not enough space. Finally, we have shown that the different patterns can be classified by appropriate quantitative indicators.

Acknowledgments. The authors DL and IS would like to thank the Isaac Newton Institute for Mathematical Sciences (Cambridge) for its hospitality during the program [Coupling Geometric PDEs with Physics for Cell Morphology, Motility and Pattern Formation] supported by EPSRC Grant Number EP/K032208/1. DL research work has been performed under the auspices of the Italian National Group for Mathematical Physics (GNFM-Indam)

Appendix A

In this appendix, we explicitly derive the eigenfunctions of the eigenvalue problem (10). To this aim, we observe that system (10) can be solved by separation of variables, searching for solutions in the form $Y(\phi,\psi) = Q(\phi)\,P(\psi)$. As a consequence, one gets

$$\frac{1}{\sin^2\psi}P(\psi)\,Q''(\phi) + Q(\phi)\,P''(\psi) + \frac{\cos\psi}{\sin\psi}P'(\psi)\,Q(\phi) + k^2\,P(\psi)\,Q(\phi) = 0,$$

that, by dividing both sides by $P(\psi)\,Q(\phi)/\sin^2\psi$, reads as:

$$\frac{Q''(\phi)}{Q(\phi)} + \frac{P''(\psi)}{P(\psi)}\,\sin^2\psi + \sin\psi\cos\psi\frac{P'(\psi)}{P(\psi)} + k^2\,\sin^2\psi = 0. \tag{51}$$

In (51), the first term is a function of ϕ and the sum of the others is a function of ψ. Hence the terms involving P and Q have to be equal to constants which sum is zero. As a consequence, for each $m = 0, \pm1, \pm2, \ldots$ we get the ordinary differential equations:

$$\frac{Q''(\phi)}{Q(\phi)} = -m^2, \tag{52}$$

equipped with periodic boundary conditions and

$$\left(k^2 - \frac{m^2}{\sin^2\psi}\right)\,P + \frac{1}{\sin\psi}\,(\sin\psi\,P')' = 0, \tag{53}$$

with P bounded at $\psi = 0$ and $\psi = \pi$. Solutions of equation (52) can be straightforwardly proved to be $Q(\phi) = \exp(i\,m\,\phi)$ whereas, as far as equation (53) is concerned, the change of variable $s = \cos\psi$ allows to obtain the so called *associated Legendre's equation*

$$\left[(1-s^2)P'(s)\right]' + \left[k^2 - \frac{m^2}{(1-s^2)}\right]\,P(s) = 0 \tag{54}$$

with $P(s)$ bounded at $s = \pm1$. By using the method of power series it is possible to show that solutions $P(s)$ (54) can be written in terms of the Legendre polynomials, i.e. $P(s) = L_l^m(s) = (1-s^2)^{m/2}\dfrac{d^m}{ds^m}L_l(s)$ where the Legendre polynomial $L_l(s)$ is given by $L_l(s) = 2^l\displaystyle\sum_{k=0}^{l} s^k \binom{l}{k}\binom{\frac{l+k-1}{2}}{l}$ and l is a positive integer number such that $l \geqslant |m|$. The eigenfunctions of the eigenvalue problem (10) are hence given by the spherical harmonics:

$$Y_l^m(\phi,\psi) = L_l^{|m|}(\cos\psi)\,\exp(i\,m\,\phi).$$

Appendix B

In this appendix, we show in more detail the derivation of the set of phenomenological kinetic equations (43). The rate equations reported in (43) can be derived according to standard

phenomenological homogeneous chemical kinetics (see, e.g. [54] pages 1-7) as the source terms of balance equations for $Zn(OH)_{2,surf}$ and $Zn\,OH_{surf}$.
Since $Zn(OH)_{2,surf}$ is generated in forwards reaction (42.a) and backwards reaction (42.b) positive contributions appear in the respective source terms (43); the same species is consumed in backwards reaction (42.a) and forwards reaction (42.b) and therefore the corresponding contributions to the source term are negative. The molecularities correspond to classical mono- and bi-molecular models (see, e.g. [54] pages 7-9) and the forwards and backwards rate constants $\vec{k}_i, \overleftarrow{k}_i$, $i = 1, 2, 3$, as customary, can be interpreted in terms of the Arrhenius model as ways to incorporate the dependence of reaction velocity on non-chemical generalized forces acting on the system. As far as the mass balance of $Zn\,OH_{surf}$ is concerned, forwards reaction (42.b) and backward reaction (42.c) generate this species, while backwards (42.b) and forwards (42.c) consume it, yielding positive and negative contributions, respectively.

References

References

[1] Banik, S., Akolkar, R., 2015. Suppressing dendritic growth during alkaline zinc electrodeposition using polyethylenimine additive. Electrochimica Acta 179, 475 – 481.

[2] Barreira, R., Elliott, C. M., Madzvamuse, A., 2011. The surface finite element method for pattern formation on evolving biological surfaces. Journal of Mathematical Biology 63 (6), 1095–1119.

[3] Barrio, R., Varea, C., Aragón, J., Maini, P., 1999. A two-dimensional numerical study of spatial pattern formation in interacting Turing systems. Bulletin of Mathematical Biology 61 (3), 483–505.

[4] Berding, C., 1987. On the heterogeneity of reaction-diffusion generated pattern. Bulletin of Mathematical Biology 49 (2), 233–252.

[5] Bockris, J. O., Nagy, Z., Damjanovic, A., 1972. On the deposition and dissolution of zinc in alkaline solutions. Journal of The Electrochemical Society 119 (3), 285–295.

[6] Bozzini, B., Altissimo, M., Amati, M., Bocchetta, P., Gianoncelli, A., Gregoratti, L., Kourousias, G., Mancini, L., Mele, C., Kiskinova, M., 2015. In situ and ex situ X-ray microspectroelectrochemical methods for the study of zinc-air batteries. In: Reference Module in Chemistry, Molecular Sciences and Chemical Engineering. Elsevier, pp. 1–21.

[7] Bozzini, B., Gambino, G., Lacitignola, D., Lupo, S., Sammartino, M., Sgura, I., 2015. Weakly nonlinear analysis of Turing patterns in a morphochemical model for metal growth. Computers & Mathematics with Applications 70 (8), 1948 – 1969.

[8] Bozzini, B., Guerrieri, M., Capotondi, F., Sgura, I., Tondo, E., 2011. Electrochemical preparation of particles for X-ray free electron laser based diffractive imaging. Int. J. Electrochem. Sci 6, 2609–2631.

[9] Bozzini, B., Lacitignola, D., Mele, C., Sgura, I., 2012. Coupling of morphology and chemistry leads to morphogenesis in electrochemical metal growth: a review of the reaction-diffusion approach. Acta Appl. Math. 122, 53–68.

[10] Bozzini, B., Lacitignola, D., Sgura, I., 2013. Spatio-temporal organization in alloy electrodeposition: a morphochemical mathematical model and its experimental validation. Journal of Solid State Electrochemistry 17 (2), 467–479.

[11] Bozzini, B., Romanello, V., Gaudenzi, G. P. D., Mele, C., 2006. Controlled corrosion of micrometric and submicrometric metal powders in fluidised bed reactor. Transactions of the IMF 84 (3), 154–158.

[12] Busse, F. H., 11 1975. Patterns of convection in spherical shells. Journal of Fluid Mechanics 72, 67–85.

[13] Callahan, T., 2004. Turing patterns with O(3) symmetry. Physica D: Nonlinear Phenomena 188 (1–2), 65 – 91.

[14] Caramia, V., Bozzini, B., 2014. Materials science aspects of zinc–air batteries: a review. Materials for Renewable and Sustainable Energy 3 (2), 1–12.

[15] Carr, J., 1981. Applications of Centre Manifold Theory. Springer, New York.

[16] Chaplain, M., Ganesh, M., Graham, I., 2001. Spatio-temporal pattern formation on spherical surfaces: numerical simulation and application to solid tumour growth. Journal of Mathematical Biology 42 (5), 387–423.

[17] Chazalviel, J., Dec 1990. Electrochemical aspects of the generation of ramified metallic electrodeposits. Phys. Rev. A 42, 7355–7367.

[18] Chen, C., Jorné, J., 1990. Fractal analysis of zinc electrodeposition. Journal of The Electrochemical Society 137 (7), 2047–2051.

[19] Cogswell, D. A., 2015. Quantitative phase-field modeling of dendritic electrodeposition. Physical Review E 92 (1), 011301.

[20] Cooper, J., Krueger, R., 2006. The refuelable zinc-air battery: Alternative techniques for zinc and electrolyte regeneration. LLNL report UCRL-TR-218414.

[21] Cruywagen, G. C., Maini, P. K., Murray, J. D., 1997. Biological pattern formation on two-dimensional spatial domains: a nonlinear bifurcation analysis. SIAM J. Appl. Math. 57 (6), 1485–1509.

[22] DeHoff, R., 2006. Thermodynamics in Materials Science. Taylor and Francis, Boca Raton.

[23] Desai, D., Turney, D., Anantharaman, B., Steingart, D., Banerjee, S., 2014. Morphological evolution of nanocluster aggregates and single crystals in alkaline zinc electrodeposition. The Journal of Physical Chemistry C 118 (16), 8656–8666.

[24] Diggle, J., Despic, A., Bockris, J., 1969. The mechanism of the dendritic electrocrystallization of zinc. J. Electrochem. Soc. 116, 1503–1514.

[25] Dziuk, G., 1988. Finite elements for the Beltrami operator on arbitrary surfaces. Partial Differential Equations and Calculus of Variations, 142–155.

[26] Dziuk, G., Elliott, C., 2013. Finite element methods for surface PDEs. Acta Numerica 22, 289–396.

[27] Dziuk, G., Elliott, C. M., 2007. Finite elements on evolving surfaces. IMA Journal of Numerical Analysis 27 (2), 262–292.

[28] Dziuk, G., Elliott, C. M., 2007. Surface finite elements for parabolic equations. Journal of Computational Mathematics -International Edition- 25 (4), 385.

[29] Frittelli, M., Madzvamuse, A., Sgura, I., Venkataraman, C., 2016. Lumped finite element method for reaction-diffusion systems on stationary closed surfaces. arXiv preprint arXiv:1609.02741.

[30] Gambino, G., Lombardo, M., Sammartino, M., 2013. Pattern formation driven by cross-diffusion in a 2D domain. Nonlinear Anal. Real World Appl. 14 (3), 1755–1779.

[31] Garvie, M. R., Burkardt, J., Morgan, J., 2015. Simple finite element methods for approximating predator–prey dynamics in two dimensions using Matlab. Bulletin of Mathematical Biology 77 (3), 548–578.

[32] Garvie, M. R., Trenchea, C., 2007. Finite element approximation of spatially extended predator–prey interactions with the Holling type II functional response. Numerische Mathematik 107 (4), 641–667.

[33] Garzon-Alvarado, D., Martinez, A., Segrera, D., 2011. A model of cerebral cortex formation during fetal development using reaction-diffusion-convection equations with Turing space parameters. Computer Methods and Programs in Biomedicine 104 (3), 489–497.

[34] Gianoncelli, A., Sgura, I., Bocchetta, P., Lacitignola, D., Bozzini, B., 2015. High-lateral resolution X-ray fluorescence microspectroscopy and dynamic mathematical modelling as tools for the study of electrodeposited electrocatalysts. X-Ray Spectrometry 44 (4), 263–275.

[35] Gilad, E., von Hardenberg, J., Provenzale, A., Shachak, M., Meron, E., Aug 2004. Ecosystem engineers: From pattern formation to habitat creation. Phys. Rev. Lett. 93, 098105.

[36] Gjorgjieva, J., Jacobsen, J., 2007. Turing patterns on growing spheres: The exponential case. Discrete and Continuous Dynamical Systems- Series A (SUPPL.), 436–445, cited By 12.

[37] Golubitsky, M., Schaeffer, D., 1985. Singularities and Groups in Bifurcation Theory - Vol. I. Springer, New York.

[38] Gowda, K., Chen, Y., Iams, S., Silber, M., 2016. Assessing the robustness of spatial pattern sequences in a dryland vegetation model. Proceedings of the Royal Society of London A: Mathematical, Physical and Engineering Sciences 472 (2187).

[39] Gowda, K., Riecke, H., Silber, M., 2014. Transitions between patterned states in vegetation models for semiarid ecosystems. Phys. Rev. E 89, 022701.

[40] Hamilton, D., 1963. A theory of dendritic growth in electrolytes. Electrochimica Acta 8 (9), 731 – 740.

[41] Lacitignola, D., Bozzini, B., Sgura, I., 2014. Spatio-temporal organization in a morphochemical electrodeposition model: Analysis and numerical simulation of spiral waves. Acta Applicandae Mathematicae 132, 377–389.

[42] Lacitignola, D., Bozzini, B., Sgura, I., 2015. Spatio-temporal organization in a morphochemical electrodeposition model: Hopf and Turing instabilities and their interplay. European Journal of Applied Mathematics 26 (2), 143–173.

[43] Liaw, S., Yang, C., Liu, R., Hong, J., 2001. Turing model for the patterns of lady beetles. Physical Review E - Statistical, Nonlinear, and Soft Matter Physics 64 (4 I), 419091–419095, cited By 31.

[44] Lu, Y., Tu, Z., Archer, L., 2014. Stable lithium electrodeposition in liquid and nanoporous solid electrolytes. Nature materials 13, 961–969.

[45] Lucas, S., Moskovkin, P., 2010. Simulation at high temperature of atomic deposition, islands coalescence, Ostwald and inverse Ostwald ripening with a general simple kinetic Monte Carlo code. Thin Solid Films 518 (18), 5355 – 5361.

[46] Madzvamuse, A., Chung, A. H. W., Venkataraman, C., 2015. Stability analysis and simulations of coupled bulk-surface reaction–diffusion systems. Proceedings of the Royal Society of London A: Mathematical, Physical and Engineering Sciences 471 (2175).

[47] Matthews, P., 2003. Transcritical bifurcation with O (3) symmetry. Nonlinearity 16 (4), 1449.

[48] Matthews, P. C., Mar 2003. Pattern formation on a sphere. Phys. Rev. E 67, 036206.

[49] McBreen, J., Cairns, E., 1978. The zinc electrode. Advances in electrochemistry and electrochemical engineering 11, 273–352.

[50] Murray, J., 2003. Mathematical Biology II - Spatial Models and Biomedical Applications. Springer-Verlag, Berlin Heidelberg.

[51] Nagata, W., Harrison, L., Wehner, S., 2003. Reaction-diffusion models of growing plant tips: Bifurcations on hemispheres. Bulletin of Mathematical Biology 65 (4), 571–607.

[52] Nicolis, G., Prigogine, I., 1977. Self-organization in nonequilibrium systems. John Wiley, New York.

[53] Othmer, H. G., Pate, E., 1980. Scale-invariance in reaction-diffusion models of spatial pattern formation. Proceedings of the National Academy of Sciences 77 (7), 4180–4184.

[54] Pilling, M., Seakins, P., 1995. Reaction Kinetics. Oxford University Press, Oxford.

[55] Plaza, R., Sánchez-Garduño, F., Padilla, P., Barrio, R., Maini, P., 2004. The effect of growth and curvature on pattern formation. Journal of Dynamics and Differential Equations 16 (4), 1093–1121.

[56] Popov, K., Djokic, S., Grgur, B., 2002. Fundamental Aspects of Electrometallurgy. Kluwer Academic, New York.

[57] Rietkerk, M., Boerlijst, M., van Langevelde, F., HilleRisLambers, R., van de Koppel, J., Kumar, L., Prins, H. T., de Roos, A., Westoby, A. E. M., 2002. Self-organization of vegetation in arid ecosystems. The American Naturalist 160 (4), 524–530.

[58] Rohlf, K., Glass, L., Kapral, R., 2006. Spiral wave dynamics in excitable media with spherical geometries. Chaos 16 (3), cited By 5.

[59] Rosen, J., Hutchings, G. S., Lu, Q., Forest, R. V., Moore, A., Jiao, F., 2015. Electrodeposited Zn dendrites with enhanced CO selectivity for electrocatalytic CO2 reduction. ACS Catalysis 5 (8), 4586–4591.

[60] Sapkota, P., Kim, H., 2009. Zinc-air fuel cell, a potential candidate for alternative energy. Journal of Industrial and Engineering Chemistry 15 (4), 445 – 450.

[61] Sattinger, D. H., 1978. Bifurcation from rotationally invariant states. Journal of Mathematical Physics 19 (8), 1720–1732.

[62] Sgura, I., Lawless, A., Bozzini, B., 2016. Parameter estimation for a morphochemical reaction-diffusion model of electrochemical pattern formation. Submitted.

[63] Shankar, V., Wright, G. B., Kirby, R. B., Fogelson, A. L., 2015. A Radial Basis Function (RBF) - Finite Difference (FD) for diffusion and reaction-diffusion equations on surfaces. Journal of Scientific Computing 63, 745–768.

[64] Sigrist, R., Matthews, P., 2011. Symmetric spiral patterns on spheres. SIAM Journal on Applied Dynamical Systems 10 (3), 1177–1211.

[65] Taylor., M. E., 2011. Partial differential equations I: Basic Theory, 2nd Ed., Series: Applied Mathematical Sciences, Vol. 115. Springer, New York.

[66] Thompson, D., 1968. On Growth and Form. Cambridge University Press, Cambridge.

[67] Trinh, P., Ward, M., 2016. The dynamics of localized spot patterns for reaction-diffusion systems on the sphere. Nonlinearity 29 (3), 766–806.

[68] Tuncer, N., Madzvamuse, A., Meir, A. J., 2015. Projected finite elements for reaction–diffusion systems on stationary closed surfaces. Appl. Num. Math. 96, 45–71.

[69] Varea, C., Aragón, J. L., Barrio, R. A., 1999. Turing patterns on a sphere. Phys. Rev. E 60, 4588–4592.

[70] von Hardenberg, J., Meron, E., Shachak, M., Zarmi, Y., 2001. Diversity of vegetation patterns and desertification. Phys. Rev. Lett. 87, 198101.

[71] Wang, K., Pei, P., Ma, Z., Chen, H., Xu, H., Chen, D., Wang, X., 2015. Dendrite growth in the recharging process of zinc-air batteries. J. Mater. Chem. A 3, 22648–22655.

[72] Wang, K., Pei, P., Ma, Z., Xu, H., Li, P., Wang, X., 2014. Morphology control of zinc regeneration for zinc-air fuel cell and battery. Journal of Power Sources 271, 65 – 75.